International Journal of Hydrogen Energy 136 (2025) 923–937

Contents lists available at ScienceDirect

International Journal of Hydrogen Energy

journal homepage: www.elsevier.com/locate/he

Computational predictions of weld structural integrity in hydrogen transport pipelines

Tushar Kanti Mandal [a,c], Jonathan Parker [b], Michael Gagliano [b], Emilio Martínez-Pañeda [a,c,*]

[a] Department of Engineering Science, University of Oxford, Oxford OX1 3PJ, UK
[b] Electric Power Research Institute, 3420 Hillview Avenue, Palo Alto, CA 94304, USA
[c] Department of Civil and Environmental Engineering, Imperial College London, London SW7 2AZ, UK

ARTICLE INFO

Keywords:
Hydrogen embrittlement
Multi-physics modelling
Phase field fracture
Pipeline steels
Welds

ABSTRACT

We combine welding process modelling with deformation–diffusion–fracture (embrittlement) simulations to predict failures in hydrogen transport pipelines. The focus is on the structural integrity of seam welds, as these are often the locations most susceptible to damage in gas transport infrastructure. Finite element analyses are conducted to showcase the ability of the model to predict cracking in pipeline steels exposed to hydrogen-containing environments. The validated model is then employed to quantify critical H_2 fracture pressures. The coupled, phase field-based simulations conducted provide insight into the role of existing defects, microstructural heterogeneity, and residual stresses. We find that under a combination of deleterious yet realistic conditions, the critical pressure at which fracture takes place can be as low as 15 MPa. These results bring new mechanistic insight into the viability of using the existing natural gas pipeline network to transport hydrogen, and the computational framework presented enables mapping the conditions under which this can be achieved safely.

1. Introduction

Driven by the prominent role that hydrogen will play as a clean energy vector, there is growing interest in assessing the suitability of transporting gaseous hydrogen through the existing natural gas pipeline network [1–4]. From a techno-economic point of view, the desire is to be able to safely and reliably move large volumes of hydrogen at the required gas purity and pressure [5,6]. However, hydrogen is known to dramatically degrade metallic materials [7–9]. Recent experimental studies have shown that exposing pipeline steels to hydrogen gas (or natural gas/hydrogen mixtures) leads to reduced fracture resistance [10–13], accelerated fatigue crack growth rates [14,15], and degraded tensile behaviour (e.g., reductions in breaking stress, notch tensile strength, ductility) [16,17]. Consequently, quantifying the factors affecting performance within a robust engineering framework will allow identifying the conditions under which hydrogen can be safely transported in existing and new pipeline infrastructure. This capability would have value for assessing the suitability of existing gas pipelines and provide benefits to new systems. Real-scale trials are ongoing, where pipeline integrity is assessed under a progressively increasing gas pressure and/or hydrogen gas purity [18,19]; however, these tests are inherently of a relatively short duration and arguably not a good representation of long-term conditions due to a number of reasons, ranging from fatigue damage to the need to destabilise the existing oxide film to enable hydrogen ingress into the pipeline steel. Moreover, there are many different steel grades used in line pipe applications. These are typically fabricated to API 5L Line Pipe specifications and are classified according to tensile properties. Thus, it is impossible to assess all the combinations of steels, welds and operating conditions using physical tests. The goal of the present work is to utilise state-of-the-art computational technologies to overcome these methodological challenges and provide a mechanistic assessment of pipeline integrity as a function of hydrogen pressure and content.

Coupled finite element models provide an avenue for predicting hydrogen diffusion and its interplay with material deformation and damage [20,21]. Typically, these models assume a given hydrogen concentration at the exposed boundaries (although some models can also quantify hydrogen uptake [22,23]), and predict the distribution of hydrogen due to diffusion, driven by gradients of concentration and of hydrostatic stress [24,25], and its sequestration at microstructural traps [26–28]. Damage is often assumed to nucleate when a critical combination of mechanical fields and hydrogen content is attained [29,30], and multiple computational technologies have been used to simulate the growth of hydrogen-assisted cracks, including cohesive zone elements [31–35], nodal release techniques [36], damage mechanics

* Corresponding author at: Department of Engineering Science, University of Oxford, Oxford OX1 3PJ, UK.
E-mail address: emilio.martinez-paneda@eng.ox.ac.uk (E. Martínez-Pañeda).

https://doi.org/10.1016/j.ijhydene.2024.01.258
Received 6 October 2023; Received in revised form 21 December 2023; Accepted 21 January 2024
Available online 25 January 2024

models [37–39], and phase field methods [40–45]. Recent years have seen significant progress in modelling abilities and it is now possible to deliver hydrogen embrittlement predictions for time and length scales of technological importance [46], effectively launching a *Virtual Testing* paradigm in hydrogen-containing environments. However, welded joints are often the weakest link in structural components and the aforementioned computational capabilities have yet to be applied to welds. Existing modelling schemes need to be extended to account for the particularities of welds (e.g., residual stresses, microstructural variations, existing defects) to deliver accurate estimations of pipeline integrity in hydrogen-containing environments.

In this work, we present a computational framework that couples weld process simulations with deformation–diffusion–fracture modelling of hydrogen-assisted cracking. The approach developed seeks to minimise the number of assumptions required and thus the integrated models perform calculations based on the engineering processes applied during fabrication and exposure. Our focus is on pipeline steels containing seam welds manufactured using submerged arc welding, so as to map safe regimes of operation in hydrogen transport pipelines. Critical pressures are determined for a wide range of scenarios to understand and quantify the role of key variables; namely: residual stresses, microstructure, weld geometry and quality, porosity, existing defects (internal and external), and hydrogen gas pressure. We find that, in the worst (realistic) scenario, H_2 pressures as low as 15 MPa can compromise the structural integrity of pipelines.

The remainder of this manuscript is structured as follows. In Section 2, the computational framework is presented, including the weld process modelling stage and the subsequent deformation–diffusion–fracture simulations, as well as their couplings. Then, the results are presented in Section 3. Residual stress states, hydrogen distributions and cracking patterns are obtained for two well-characterised seam weld configurations under varying conditions. The quantitative nature of these predictions is strengthened by the ability of the model to predict crack growth resistance behaviour (R-curves) in pipeline steels (X52 and X80), showing a very good match with experiments (see Appendix). The manuscript ends with concluding remarks in Section 4.

2. Modelling framework

As sketched in Fig. 1, we present a framework that combines weld process modelling and coupled deformation–diffusion–fracture simulations. The focus is on pipelines containing seam welds manufactured using the submerged arc process and exposed to a hydrogen gas pressure p. The weld domain can be divided into three distinct regions: the base metal, the weld metal and the heat affect zone (HAZ). Using established convention, the weld metal is considered the region where complete melting and solidification have taken place, the HAZ describes the extent of the base metal where the heat from welding modifies the original microstructure, and the base metal is the region being unaffected by the welding process carried out. As depicted in Fig. 1, the first stage (weld process modelling) is needed to determine the initial stress/strain state of the weld (residual stresses, plastic strain distribution). Then, stage II simulations (embrittlement) can be conducted and cracking can be predicted as a function of the hydrogen gas pressure and relevant weld characteristics. In the following, we describe the theory underlying the weld process modelling (Section 2.1) and the coupled deformation–diffusion–fracture simulations (Section 2.2), as well as provide details of the numerical implementation (Section 2.3).

2.1. Weld model

We idealise the welding process as a thermo-mechanical problem. On the weld domain Ω, the independent variables necessary for the description of the model at each point $\mathbf{x}$ and time t are the temperature $T(\mathbf{x},t)$ and the displacement field describing the mechanical deformation of the solid $\mathbf{u}(\mathbf{x},t)$. The thermal sub-problem is characterised by the heat equation, which reads,

$$\begin{aligned} &\rho c\frac{\partial T}{\partial t}+\nabla\cdot(-k\nabla T)=0 \quad \text{in } \Omega,\\ &T=T^{*} \ \text{ on } \partial\Omega_T, \quad -k\nabla T\cdot\mathbf{n}=q_c+q_r \quad \text{on } \partial\Omega_q, \end{aligned} \tag{1}$$

where ρ, c, and k are the mass density, specific heat, and heat conductivity of the material, respectively. We consider convective and radiative cooling of the weldment from all external surfaces $\partial\Omega_q$ which includes the inner and outer surface of the pipe as well as the weld-base interfaces exposed to the air. The convective cooling is defined using Newton's law $q_c = h_c(T - T_0)$, with room temperature T_0 and heat transfer coefficient h_c. The radiative heat loss from all external surfaces is modelled using $q_r = \varepsilon_0\sigma_0\left((T - T_{\text{abs}})^4 - (T_0 - T_{\text{abs}})^4\right)$ with emissivity ε_0, Stefan–Boltzmann constant σ_0 and absolute temperature T_{abs}. Moreover, we consider the initial temperature of the weld beads to be the melting point of the material i.e., $T(\mathbf{x},0) = T_{\text{melt}}$ and that of the base metal to be the room temperature $T(\mathbf{x},0) = T_0$. Considered values of these model parameters are listed in Table 1. Furthermore, the welding process involves the addition of welding beads in stages along with introducing suitable temperature boundary conditions $T = T^{*}(t)$ at the weld cavity $\partial\Omega_T$, these specific details are discussed in Section 3.1.1.

Table 1
Model parameters for thermal problem.

h_c [W m^{-2} K^{-1}]	σ_0 [W m^{-2} K^{-4}]	ε_0 [–]	T_0 [°C]	T_{melt} [°C]	T_{abs} [°C]
25	5.69×10^{-8}	0.8	20	1500	−273

Assuming a small strain formulation, the local deformation of the solid is characterised by infinitesimal strain,

$$\boldsymbol{\varepsilon} := \nabla^{\text{sym}}\mathbf{u} = \frac{1}{2}\left(\nabla\mathbf{u} + (\nabla\mathbf{u})^{T}\right) \tag{2}$$

which is additively decomposed into thermal ($\boldsymbol{\varepsilon}_T$), elastic ($\boldsymbol{\varepsilon}_e$) and plastic ($\boldsymbol{\varepsilon}_p$) components; $\boldsymbol{\varepsilon} = \boldsymbol{\varepsilon}_e + \boldsymbol{\varepsilon}_p + \boldsymbol{\varepsilon}_T$. The thermal strain $\boldsymbol{\varepsilon}_T$ is computed using the temperature distribution obtained from the thermal sub-problem,

$$\boldsymbol{\varepsilon}_T(\mathbf{x},t) := \alpha\boldsymbol{I}(T(\mathbf{x},t) - T_0(\mathbf{x})), \tag{3}$$

where α is the coefficient of thermal expansion, T_0 denotes the room temperature, and $\boldsymbol{I}$ is the second-order unit tensor. The kinematics of plasticity are defined by the accumulated plastic strain $\varepsilon_p(\mathbf{x},t) := \int_t |\dot{\boldsymbol{\varepsilon}}_p(\mathbf{x},t')|\mathrm{d}t'$. Von-Mises plasticity with power law hardening is considered and ε_p is computed using a conventional return mapping procedure [47]. The elastic strain generates the Cauchy stress $\boldsymbol{\sigma}$ which satisfies the global momentum balance. Thus, the mechanical sub-problem of the elastoplastic solid is written as,

$$\begin{aligned} &\nabla\cdot\boldsymbol{\sigma}=\mathbf{0} \quad \text{in } \Omega, \quad \boldsymbol{\sigma}\cdot\mathbf{n}=\mathbf{0} \quad \text{on } \partial\Omega,\\ &\boldsymbol{\sigma}=\mathbb{E}:\left(\boldsymbol{\varepsilon}-\boldsymbol{\varepsilon}_p-\boldsymbol{\varepsilon}_T\right), \quad \|\boldsymbol{\sigma}_{\text{dev}}\|=\sigma_y\left(1+\frac{E\varepsilon_p}{\sigma_y}\right)^{n} \ \text{ if } \dot{\varepsilon}_p>0, \end{aligned} \tag{4}$$

with deviatoric stress $\boldsymbol{\sigma}_{\text{dev}} := \left(\boldsymbol{\sigma} - \frac{1}{3}\text{tr}\boldsymbol{\sigma}\boldsymbol{I}\right)$, fourth-order elasticity tensor $\mathbb{E}$, Young's modulus E, yield strength σ_y, and hardening exponent n.

We assume the considered thermo-mechanical problem is weakly coupled where the temperature changes can cause volumetric deformation whereas the thermal processes are unaffected by the deformation of the solid. Therefore, we have considered a sequential thermo-mechanical procedure with two field variables, temperature T and displacement $\mathbf{u}$. Accordingly, the temperature profile obtained by solving the heat equation, Eq. (1), is transferred to the mechanical sub-problem, Eq. (4), as an initial field, so as to calculate the thermal strain, Eq. (3). The temperature dependence of the thermal and mechanical material

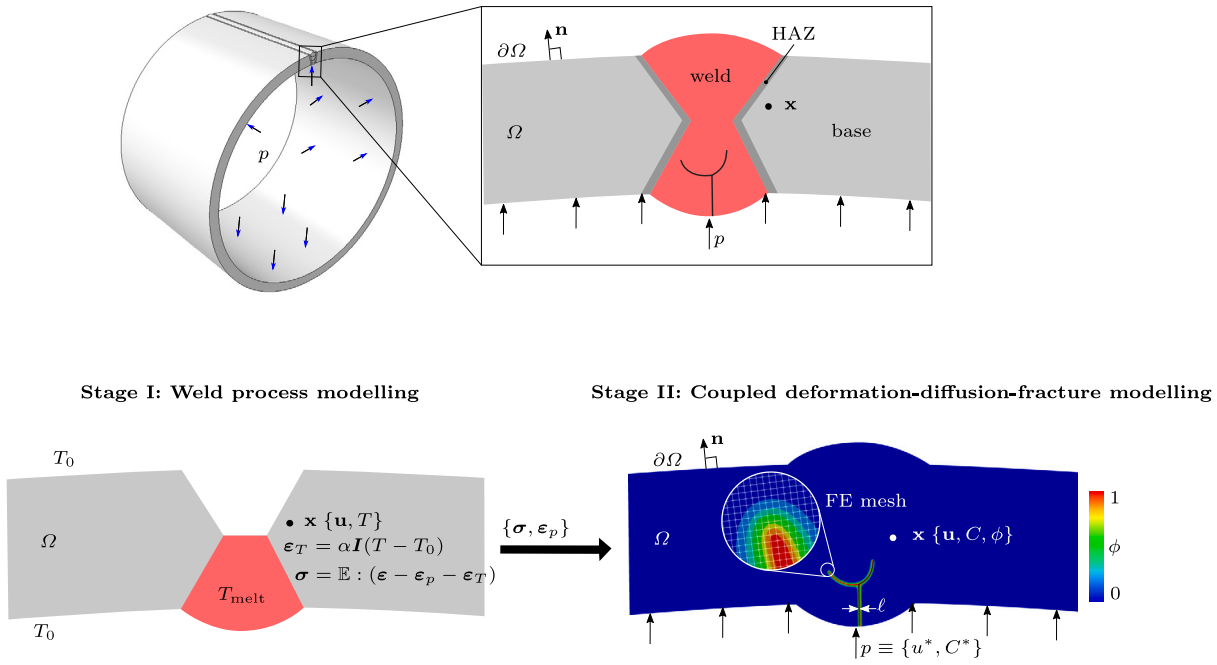

Fig. 1. Schematic representation of the finite element modelling framework, aimed at predicting hydrogen-assisted failures of welded joints in pipelines subjected to an internal hydrogen pressure p. The first stage of the modelling framework handles the simulation of the welding process, as illustrated here with one weld bead at initial melting temperature T_{melt}. The second stage uses a coupled, multi-physics phase field formulation to represent the nucleation and growth of cracks, as assisted by hydrogen.

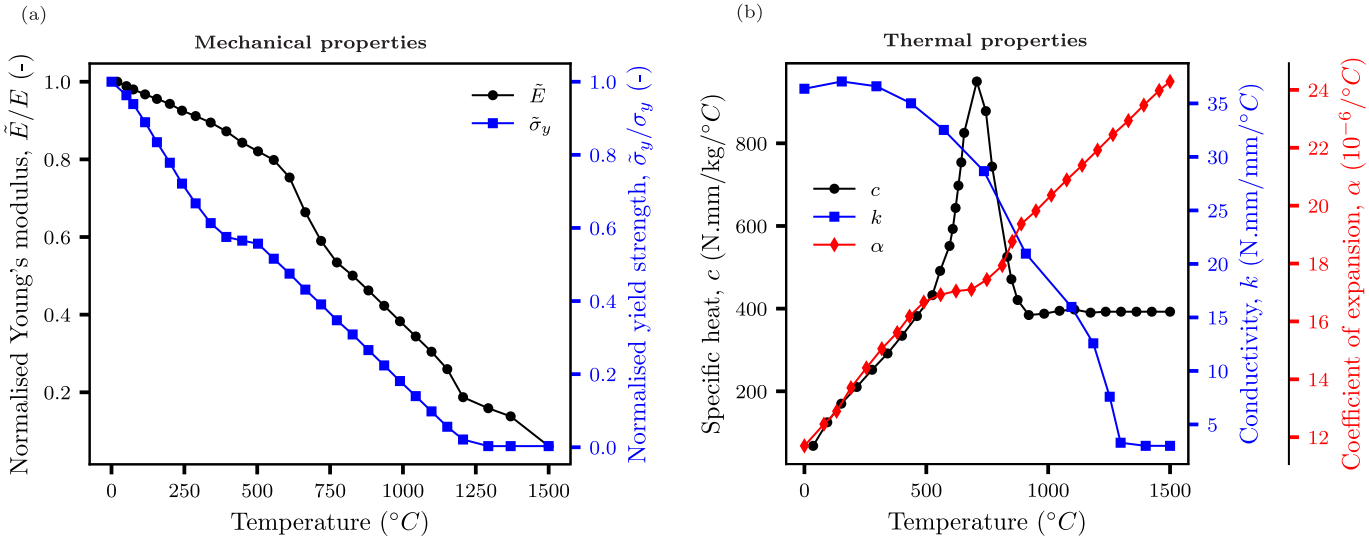

Fig. 2. Temperature-dependence of the material properties of carbon steel SA-516 Grade 70, as per ASME, Section 2, Part D [48]. The normalised mechanical properties are presented in (a), where E and σ_y denote Young's modulus and yield strength at room temperature, respectively, and $\tilde{\square}$ represents the corresponding temperature-dependent parameter. The temperature dependence of the thermal properties (specific heat c, conductivity k, coefficient of thermal expansion α) is given in (b).

properties are given in Fig. 2, following the ASME standard (Section 2, Part D) [48]. The data presented show a monotonic reduction of elastic modulus and yield strength with temperature (Fig. 2a). In addition, see Fig. 2b, the thermal conductivity reduces with increasing temperature, whereas the opposite is true for the coefficient of thermal expansion. The specific heat initially increases with temperature up to 700 °C and then decreases rapidly to reach an almost constant value.

2.2. Coupled deformation–diffusion–fracture model

We idealise the hydrogen-assisted failure of the welded joint as a coupled deformation–diffusion–fracture problem, where the evolving fracture surface is modelled using the phase field method. The variational framework for phase field and its connection with the thermodynamics of fracture are given in Section 2.2.1. The particularisation of the model to elastic–plastic fracture is then provided in Section 2.2.2, and its subsequent coupling with hydrogen transport is described in Section 2.2.3. Finally, the model is enhanced with a phenomenological degradation law for pipeline steels, which is provided in Section 2.2.4.

2.2.1. Variational framework

The phase field fracture model is based on Griffith's thermodynamics framework [49], which states that crack growth will occur when a critical strain energy release rate is attained. Considering a deformable

solid with strain energy $\Psi(\boldsymbol{\varepsilon})$, the variation of the total potential energy $\mathscr{E}$ due to an incremental increase in the crack area $\mathrm{d}A$ is given by,

$$\frac{\mathrm{d}\mathscr{E}}{\mathrm{d}A} = \frac{\mathrm{d}\Psi(\boldsymbol{\varepsilon})}{\mathrm{d}A} + \frac{\mathrm{d}W_c(C)}{\mathrm{d}A} = 0, \tag{5}$$

where the strain tensor $\boldsymbol{\varepsilon}$ characterises the local deformation and W_c is the work required to create new surfaces. The term $\mathrm{d}W_c/\mathrm{d}A$ is also known as the critical energy release rate G_c, a material property that characterises the fracture resistance. This fracture energy is known to be dependent, and very sensitive, to the hydrogen concentration C [50]. Accordingly, Griffith's energy balance can be formulated in a variational form as follows [51]

$$\mathscr{E} = \int_\Omega \psi(\boldsymbol{\varepsilon})\mathrm{d}\Omega + \int_\Gamma G_c(C)\mathrm{d}\Gamma, \tag{6}$$

with strain energy density ψ and crack surface Γ. Cracking phenomena can then be predicted as an exchange of stored and fracture energies by minimising Eq. (6). However, this requires tracking the crack surface Γ, which is computationally very challenging [52]. The phase field paradigm provides the necessary framework to predict any arbitrary evolving fracture surface by regularising it using an order parameter ϕ, which provides a smooth interface between the damaged solid ($\phi = 1$) and intact solid ($\phi = 0$). Upon a suitable choice for the crack surface density function γ, the Griffith functional (Eq. (6)) can be approximated by means of the following regularised functional [53,54],

$$\begin{aligned} \mathscr{E}_\ell &= \int_\Omega g(\phi)\psi_0(\boldsymbol{\varepsilon})\mathrm{d}\Omega + \int_\Omega G_c(C)\gamma(\phi,\ell)\mathrm{d}\Omega, \\ \gamma(\phi,\ell) &= \left(\frac{\phi^2}{2\ell} + \frac{\ell}{2}|\nabla\phi|^2\right). \end{aligned} \tag{7}$$

Here, ℓ is a length scale parameter that governs the size of the fracture process zone, ψ_0 denotes the strain energy density of the undamaged solid, and $g(\phi)$ is a degradation function. It can be shown through Gamma-convergence that $\mathscr{E}_\ell$ converges to $\mathscr{E}$ when $\ell \to 0$ [55].

2.2.2. Elastoplastic fracture

Similar to our weld model (Section 2.1), we consider a small strain formulation where the local deformation is characterised by the infinitesimal strain $\boldsymbol{\varepsilon} := \nabla^{\mathrm{sym}}\mathbf{u}$, and it is additively decomposed into the elastic ($\boldsymbol{\varepsilon}_e$) and plastic ($\boldsymbol{\varepsilon}_p$) components, as $\boldsymbol{\varepsilon} = \boldsymbol{\varepsilon}_e + \boldsymbol{\varepsilon}_p$. We define the strain energy density of the elastoplastic solid as,

$$\begin{aligned} \psi &:= g(\phi)\psi_e^+(\boldsymbol{\varepsilon}_e) + \psi_e^-(\boldsymbol{\varepsilon}_e) + \bar{g}(\phi)\psi_p(\varepsilon_p), \\ \psi_e^+ &= \frac{\mathcal{K}}{2}\langle \mathrm{tr}\boldsymbol{\varepsilon}_e\rangle^2 + \mathcal{G}\boldsymbol{\varepsilon}_e^{\mathrm{dev}} : \boldsymbol{\varepsilon}_e^{\mathrm{dev}}, \quad \psi_e^- = \frac{\mathcal{K}}{2}\langle -\mathrm{tr}\boldsymbol{\varepsilon}_e\rangle^2, \\ \psi_p &= \frac{\sigma_y^2}{E(n+1)}\left(1 + \frac{E\varepsilon_p}{\sigma_y}\right)^{(n+1)}, \end{aligned} \tag{8}$$

where $\mathcal{K}$ is the bulk modulus, $\mathcal{G}$ denotes the shear modulus, and the strain energy density is divided into its elastic (ψ_e) and plastic (ψ_p) parts, which are degraded using distinct degradation functions: $g(\phi)$ and $\bar{g}(\phi)$, respectively. Quadratic degradation functions are employed, such that

$$g(\phi) = (1-\phi)^2, \quad \bar{g}(\phi) := \beta g(\phi) + (1-\beta), \quad 0 \le \beta \le 1, \tag{9}$$

where β is a parameter that quantifies the amount of plastic work that is stored in the material. Following the seminal work by Taylor and Quinney [56], we adopt a value of $\beta = 0.1$, as only 10% of the plastic work does not dissipate as heat and is therefore available to create new fracture surfaces. Hence, the model remains consistent with the thermodynamics of fracture while accounting for the role of plasticity in dissipation and in driving crack growth. Also, the definition of $\bar{g}(\phi)$ adopted ensures variational consistency. In addition, we adopt the so-called volumetric–deviatoric split [57] to decompose the elastic strain energy so as to prevent cracking from nucleating in regions of compressive stress states. As in the welding process modelling stage, we assume elastic–plastic behaviour described by Von Mises plasticity with power law hardening. Considering also an isotropic degradation of the stress [58], the variation of the energy functional $\mathscr{E}_\ell$ with respect to the displacement $\delta\mathbf{u}$ renders

$$\begin{aligned} &\nabla\cdot\boldsymbol{\sigma} = \mathbf{0}, \qquad \boldsymbol{\sigma} = g(\phi)\mathbb{E} : \left(\boldsymbol{\varepsilon} - \boldsymbol{\varepsilon}_p\right), \\ &\|\boldsymbol{\sigma}_{\mathrm{dev}}\| = \bar{g}(\phi)\sigma_f(\varepsilon_p) \ \text{ if } \dot{\varepsilon}_p > 0, \quad \sigma_f(\varepsilon_p) := \sigma_y\left(1 + \frac{E\varepsilon_p}{\sigma_y}\right)^n. \end{aligned} \tag{10}$$

While by taking the variation of the energy functional $\mathscr{E}_\ell$ with respect to the phase field $\delta\phi$ one reaches

$$\nabla^2\phi = \left(\frac{\phi}{\ell^2} + g'(\phi)\frac{\mathcal{H}}{\ell G_c}\right), \quad \mathcal{H} := \max\left(\max\left(\psi_e^+, \psi_{e(t)}^+\right) + \beta\psi_p\right), \tag{11}$$

where damage irreversibility has been enforced by adopting a non-decreasing crack driving energy $\mathcal{H}$ [59]. It is also worth noting that the phase field length scale parameter is directly related to the fracture strength $\hat{\sigma}$ as [60],

$$\ell = \frac{27}{256}\frac{EG_c}{\hat{\sigma}^2}. \tag{12}$$

2.2.3. Hydrogen transport

We describe the diffusion of hydrogen through the crystal lattice by employing the usual Fickian model for the hydrogen flux $\mathbf{J}$, such that

$$\frac{\partial C}{\partial t} = -\nabla\cdot\mathbf{J}, \quad \text{with} \quad \mathbf{J} = -\frac{DC}{RT}\nabla\mu, \tag{13}$$

with (apparent) hydrogen diffusion coefficient D, ideal gas constant $R = 8.314$ J/(mol K), and absolute temperature T. We define the chemical potential μ assuming that the hydrogen resides in interstitial lattice sites of steel as a diluted species,

$$\mu = \mu^0 + RT\ln\left(\frac{\theta_L}{1-\theta_L}\right) - \bar{V}_H\sigma_h, \tag{14}$$

where μ^0 is the reference chemical potential, $\sigma_h := \mathrm{tr}\boldsymbol{\sigma}/3$ is the hydrostatic stress, and $\bar{V}_H$ is the partial molar volume of hydrogen in solid solution, which takes a value of 2000 mm^3/mol in iron-based materials. Also, $\theta_L = C/N_L$ is the lattice occupancy, a function of the lattice hydrogen concentration and the lattice site density N_L. The role of traps is here accounted for by taking D to be the effective diffusion coefficient, but the model can readily be extended to explicitly consider multiple trap types (see Ref. [28]).

It is also necessary to handle the interplay between hydrogen transport and crack growth. It is expected that the hydrogen gas will very promptly occupy the space created by crack advance, exposing the newly created crack surfaces to the environmental hydrogen concentration. Accordingly, the diffusivity of material points in the damaged region is enhanced by making use of an amplification coefficient $k_d \gg 1$ and a damage threshold, ϕ_{th}, above which the hydrogen environment is assumed to expand. Then, the hydrogen diffusion coefficient can be expressed as,

$$D = D_0\left(1 + k_d\langle\phi - \phi_{\mathrm{th}}\rangle\right) \tag{15}$$

where D_0 is the hydrogen diffusivity of the undamaged material and $\langle\square\rangle$ are Macaulay brackets. In this regard, it should be noted that ϕ_{th} denotes the damage threshold above which an interconnected network of cracks is assumed to exist, such that the hydrogen can find its way from the environment. Exploiting the analogy between phase field and damage mechanics, we assume $\phi_{\mathrm{th}} \approx 0.8$ to be a sensible choice (microcracks occupy 80% of the surface plane). On the other side, k_d is a numerical parameter that should be taken to be as large as possible. We find that $k_d \approx 10^4$ delivers a robust model and is sufficient to achieve the desired effect. The reader is referred to Ref. [61] for further details of this approach and its numerical implementation, and to Ref. [62] for a discussion on alternative approaches such as penalty-based *moving* chemical boundary conditions.

Table 2
Material parameters characterising the behaviour of pipeline steels (X52, X80) in the presence of hydrogen. $J_{Ic}(0)$ denotes the measured value of J_{Ic} in the absence of hydrogen, $J_{Ic}^{\min}$ is the lowest value of J_{Ic} measured for that material in a hydrogen-containing environment, and q_1 and q_2 are fitting parameters in Eq. (17).

Steel	σ_y [MPa]	$J_{Ic}(0)$ [N/mm]	$J_{Ic}^{\min}$ [N/mm]	q_1 [–]	q_2 [–]
X80	660	289	20	9	0.8
X52	430	400	50	25	2

2.2.4. Hydrogen degradation function

It remains to define the dependency of the fracture energy upon the hydrogen content. To this end, a hydrogen degradation function $f(C)$ has to be defined, such that,

$$G_c(C) = f(C)G_c(0) \tag{16}$$

where $G_c(0)$ is the critical energy release in a hydrogen-free environment. Several approaches can be adopted here, including mechanistic ones (e.g., using atomistic predictions of surface energy reduction with hydrogen coverage [40]) and phenomenological ones. Since the relationship between fracture energy and hydrogen content is well characterised in pipeline steels, we choose to adopt a phenomenological approach. To this end, an analogy can be established between the J integral and the energy release rate G under the assumption of small scale yielding conditions, with G_c being the value of J at which crack growth initiates (see Appendix for details). Experimental data exists characterising the drop of fracture energy with hydrogen content for pipeline steels - Fig. 3 shows a collection of published data for X52 and X80 pipeline steels. The data is provided for the critical value of J under mode I fracture conditions (J_{Ic}), which is measured for a crack extension of 0.2 mm. As shown by the curves in Fig. 3, the data can be fitted through the following exponential function,

$$J_{Ic}(C) = f(C)J_{Ic}(0) = \left[\frac{J_{Ic}^{\min}}{J_{Ic}(0)} + \left(1 - \frac{J_{Ic}^{\min}}{J_{Ic}(0)}\right)\exp\left(-q_1 C^{q_2}\right)\right] J_{Ic}(0) \tag{17}$$

where q_1 and q_2 are fitting parameters, and $J_{Ic}^{\min}$ is the saturation magnitude, the lowest value of J_{Ic} in hydrogen-containing environments. The values of q_1 and q_2 that provided the best fit to the experimental data are given in Table 2, together with the measured values of J_{Ic}, $J_{Ic}^{\min}$, and yield strength σ_y. As shown in Appendix, these choices are found to accurately reproduce the crack growth resistance of pipeline steels in the presence of hydrogen. Appendix also discusses the role of fracture strength $\hat{\sigma}$ in influencing the degree of plastic dissipation with crack growth. It should be noted that the fracture energy versus hydrogen content data available for pipeline steels refers mostly to the base metal. Some data exists for weld metal suggesting a similar behaviour [63] and thus the same degradation law, Eq. (17), is here adopted to describe the hydrogen degradation of material points in the weld, base and HAZ regions, albeit with different coefficients. Nevertheless, a more detailed experimental quantification would be very helpful in reducing modelling uncertainties.

2.3. Numerical implementation

We numerically implement the thermo-mechanical model of the welding process (Section 2.1) and the coupled deformation–diffusion–fracture model for welded joints (Section 2.2) using the commercial finite element package `Abaqus`. Several user subroutines were developed. For the welding process modelling, a user material (`UMAT`) subroutine is used to implement power law temperature-dependent elastoplasticity, extending the code provided in Ref. [71]. The welding sequence is modelled by removing all the elements in the weld region at the beginning of the simulation and then progressively adding (or activating) the elements corresponding to each weld bead. This is achieved using the '*Model Change' feature in `Abaqus`. Moreover, the required temperature boundary conditions corresponding to each weld pass are automated using a welding interface plugin [72]. The residual stresses and strains computed in the weld process modelling stage are provided as input to the coupled deformation–diffusion–fracture simulations using a `SDVINI` subroutine. Specifically, we transfer the accumulated plastic strain, and the elastic and plastic parts of the strain tensor ($\epsilon_p, \boldsymbol{\epsilon}_e, \boldsymbol{\epsilon}_p$) as the initial values. In regards to the hydrogen-assisted fracture simulations, a `UMAT` subroutine is developed to couple elastic–plastic constitutive behaviour and phase field fracture. The implementation exploits the analogy between the heat equation and the phase field evolution equation, extending to elastic–plastic solids the work by Navidtehrani et al. [73,74]. Hydrogen transport is simulated using a user element (`UEL`) subroutine, where the gradient of hydrostatic stress is computed by an extrapolation-based method [75,76]. The `UMAT` and `UEL` subroutines are coupled using Fortran modules. The codes developed and pre-/post-processing Python scripts with examples are available for download at https://www.empaneda.com/codes/.

3. Results

As shown in Appendix, the coupled deformation–diffusion–fracture model presented in Section 2.2 can accurately capture the crack growth resistance of X52 and X80 pipeline steels in air and hydrogen-containing environments. This validated model is now coupled with welding process simulations and used to gain insight into the structural integrity of seam (i.e., longitudinal) welds in a representative pipeline with an inner radius of 110 mm and thickness of 7.5 mm. As shown in Fig. 4, the pipeline contains a seam weld that is symmetrically positioned at the top of the pipeline section. We shall consider two weld configurations, based on images of seam welds from gas transport pipelines taken out of service. The two welds, shown in Fig. 4, are representative of submerged arc welded joints typical of pipelines considered for hydrogen transport and span a relevant range of seam weld configurations and geometries. The first weld to be considered is a two-pass seam weld (Section 3.1), while the second one is a three-pass weld. Detailed microstructure (hardness) information is available (see Fig. 4), allowing us to investigate the influence of spatially-varying properties (Section 3.2). These two realistic weld configurations are used to quantify the critical pressures at which hydrogen-assisted fractures compromise the structural integrity of the pipeline and to investigate the role of weld geometry, existing defects, porosity, residual stresses, weld/base metal mismatch, weld process (number of passes), and microstructural heterogeneity. In both cases, simulations were conducted for two pipeline steels: X52 and X80. The material properties employed for each steel are given in Table 3.

The material properties have been chosen based on experimental measurements from the literature and current understanding of weld region characterisation. The Young's modulus of the weld is usually higher than that of the base metal [77], and accordingly is here taken to be 5% higher than that of the base metal. The weld is usually stronger and comparatively brittle compared to the base metal due to the thermal loading history; therefore we have considered the yield strength of the weld to be 10% higher than that of the base metal, whereas the fracture energy is 10% lower. In regards to the work hardening capacity, studies on pipeline steels report a higher magnitude for the base metal relative to the weld material [63], and accordingly, this is accounted for by using a lower hardening exponent n for the weld ($n = 0.1$ vs. $n = 0.05$). The diffusivity values of hydrogen in pipeline steel for both weld and base metal are taken from Ref. [78]. The fracture energy and fracture strength parameters, and their sensitivity to hydrogen concentration, are introduced following the experimental data and simulations presented in Section 2.2.4 and Appendix. Plane strain conditions are assumed.

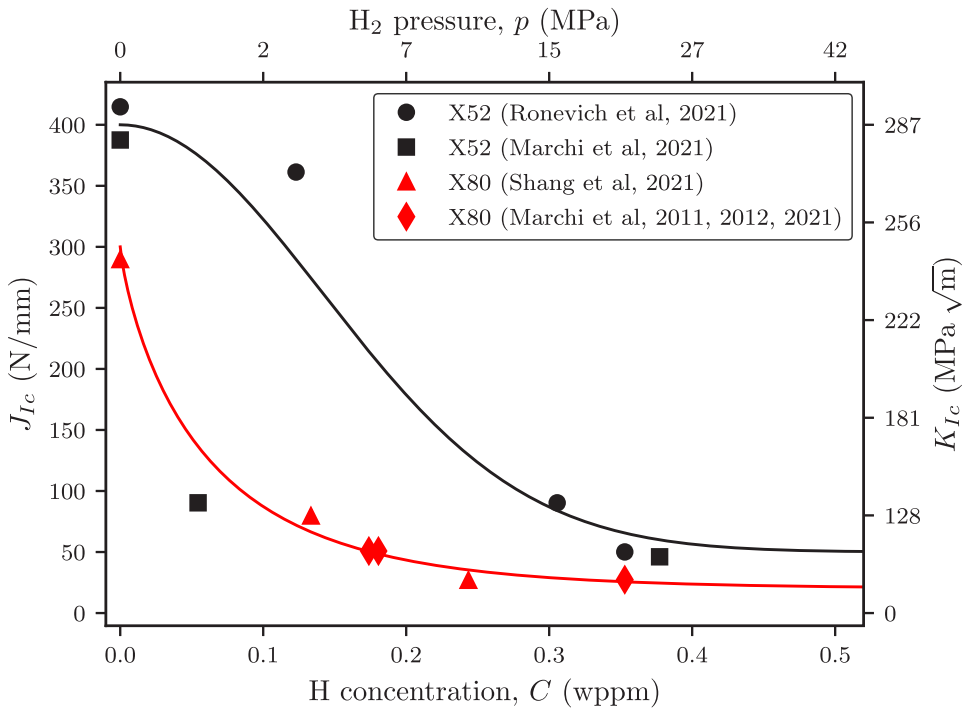

Fig. 3. Hydrogen-dependent critical fracture energy for API steels: X52 [64,65], X80 [66–69]. The fitted curves are obtained using Eq. (17) with fitting parameters listed in Table 2. For convenience, the corresponding critical stress intensity factor K_{Ic} is added on the right and it is related to J_{Ic}, as $K_{Ic} = \sqrt{E' J_{Ic}}$ with $E' = E/(1-\nu^2)$ for plane strain conditions. Also the corresponding hydrogen pressure p is added on top; lattice hydrogen concentration C and hydrogen pressure p are related via Sievert's law $C = S\sqrt{p}$, with the solubility of steel taken to be $S = 0.077$ wppm MPa$^{-0.5}$ [70].

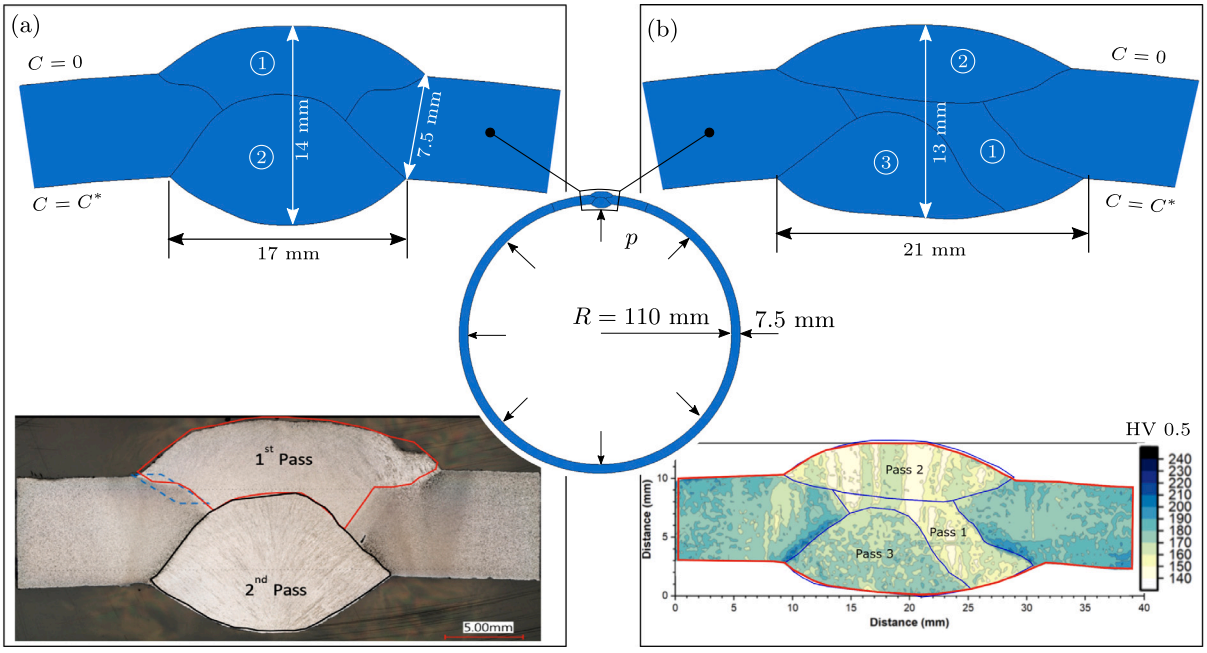

Fig. 4. Schematic representation of the boundary value problem considered, a pipeline containing a longitudinal weld. Two weld configurations were employed based on images of ex-service welds from natural gas pipelines: (a) a two-pass weld of dimensions 17 × 14 mm, and (b) a three-pass weld of dimensions 21 × 13 mm. The microstructural heterogeneity of the second weld was characterised using a Vickers Hardness (VH) mapping approach. The associated chemical boundary conditions, including the internal exposure to a hydrogen concentration C^*, are also displayed.

3.1. Case study 1: two-pass seam weld

We begin our analysis by describing the weld process simulation in the two-pass weld (Section 3.1.1), and then proceed to predict the critical pressure at which hydrogen compromises the structural integrity of the weld, considering the role of residual stresses, weld porosity, and the presence of internal and external defects (Section 3.1.2).

3.1.1. Welding residual stress

The simulation steps of the two-pass welding process are sketched in Fig. 5a. This involves applying temperature boundary conditions at

Table 3
Material parameters adopted for the weld and base metal regions of the X52 and X80 pipeline steels used in the analyses.

		E (MPa)	ν (–)	σ_y (MPa)	n (–)	$G_c(0)$ (N/mm)	$G_c^{\min}$ (N/mm)	ℓ (mm)	D (mm^2/s)
X80	Base	187 000	0.3	660	0.10	60	7	0.17	4.5×10^{-4}
	Weld	196 350	0.3	726	0.05	54	6.3	0.13	3×10^{-4}
X52	Base	187 000	0.3	430	0.10	60	16	0.40	4.5×10^{-4}
	Weld	196 350	0.3	473	0.05	54	14.4	0.31	3×10^{-4}

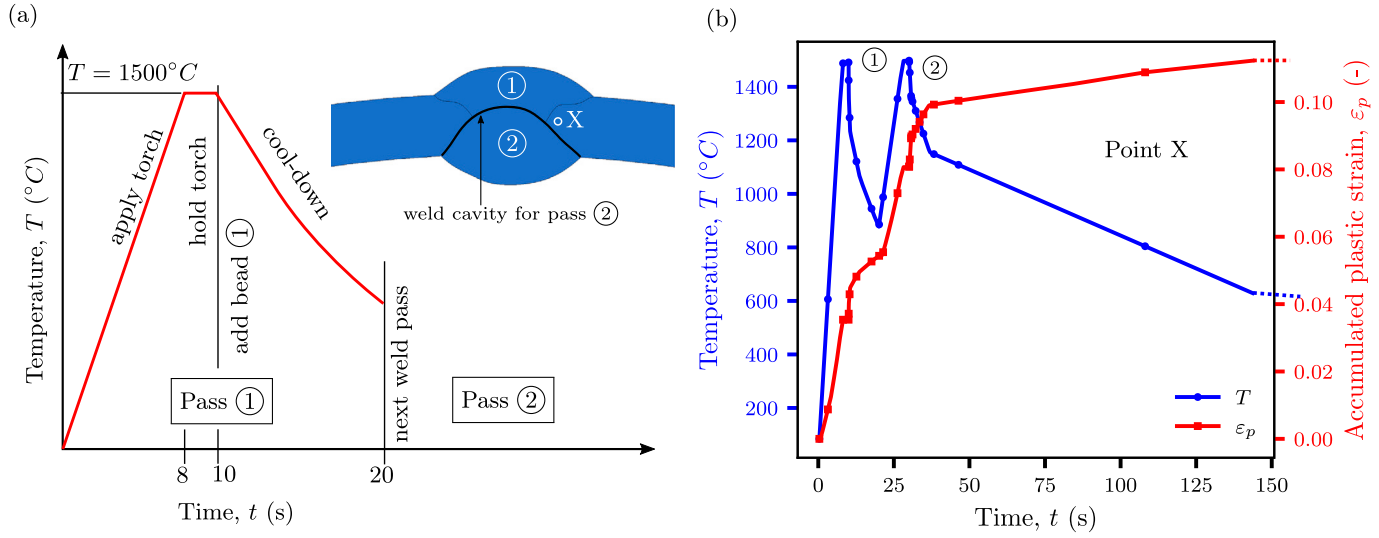

Fig. 5. Two-pass weld welding process modelling: (a) schematic representation of the temperature boundary conditions for a two-pass weld; and (b) thermal loading history and corresponding accumulated plastic strain at point 'X' near the weld. Only the first 150 s are shown but the simulation is continued until reaching room temperature (20 °C).

the weld cavity, followed by adding molten weld bead (at 1500 °C), and allowing it to cool down for 10 s before applying temperature boundary conditions at the weld cavity for the next weld pass. This is implemented as a sequential thermal–mechanical simulation in `Abaqus` (see Section 2).

A typical material point close to the weld experiences changes in mechanical fields as a result of the thermal load cycles. This is shown in Fig. 5b for a representative material point near the weld. As it can be observed, each weld pass brings a peak in temperature and the associated thermal expansions and contractions generate thermal residual stresses. This, together with the temperature dependence of the mechanical properties (Fig. 2a), results in material yielding and in a monotonic increase in accumulated plastic strain until the room temperature plateau is reached. The spatial variation of residual stresses and strains at different stages of the welding process is presented in Fig. 6. During the application of the welding torch and the addition of molten weld metal for the first pass (Fig. 6a–b), the temperature increases significantly over a region wider than the weld domain, which results in thermal expansion and corresponding compression in the circumferential direction. This is accompanied by the accumulation of plasticity near the weld cavity (i.e., near the location of the torch) due to the thermal gradient and the corresponding reduction of yield strength with increasing temperature (see Fig. 6a–b). The pipeline section then experiences circumferential tensile stretching at the periphery due to the cooling of the weld bead for the first pass (Fig. 6c). The application of the torch at the weld cavity and the addition of molten weld metal for pass 2 reverses the circumferential stress state in the pipeline section (see Fig. 6d–e) and brings as well a significant accumulation of plasticity along the HAZ. The plastic region is further expanded due to the thermal contraction that takes place during the final cooling stage (Fig. 6f). This results in tensile and compressive circumferential stresses at, respectively, the inner and outer faces of the pipeline, following the curvature of the pipeline geometry. The heterogeneous nature of the weld is thus characterised in this first case study through the different properties of base and weld metals, as listed in Table 3, and through the initial residual stress/strain distribution resulting from the welding process. This is unlike the second case study, where a hardness map is available that enables assessing the role of microstructural heterogeneities such as the influence of varying properties along the HAZ region.

3.1.2. Hydrogen embrittlement predictions

The embrittlement and fracture resistance of the welded pipeline are characterised by subjecting the welded pipeline section to a monotonically increasing hydrogen pressure p. This was simulated by applying, as Dirichlet boundary conditions, an incremental hydrogen concentration C^* and radial displacement u_r^* at the inner face of the pipe. The former is determined by making use of Sievert's law, such that,

$$C^* = S\sqrt{p}, \tag{18}$$

where the solubility of hydrogen in steel is $S = 0.077$ wppm MPa$^{-0.5}$ [70]. While the radial displacement is defined by exploiting the linear elastic relation between pressure and radial displacement of a thin cylinder [79],

$$u_r^* = \frac{pR^2}{bE}\left(1 - \frac{\nu}{2}\right), \tag{19}$$

where R is the inner radius of the pipeline and b is the pipeline thickness. A very slow loading rate of 21 Pa/s was adopted to be on the conservative side and suppress rate effects. At the outer surface, a boundary condition of $C = 0$ was adopted, as the outer surface of transport pipelines is typically exposed to environments with negligible hydrogen content. As gas transport pipelines are designed to carry out pressures below the plastic yielding of the material, we consider two potential outcomes: failure due to plastic yielding or failure due to cracking. The yielding pressure can be estimated analytically from the pipeline dimensions as,

$$p_y = \frac{\sigma_y b}{R} \tag{20}$$

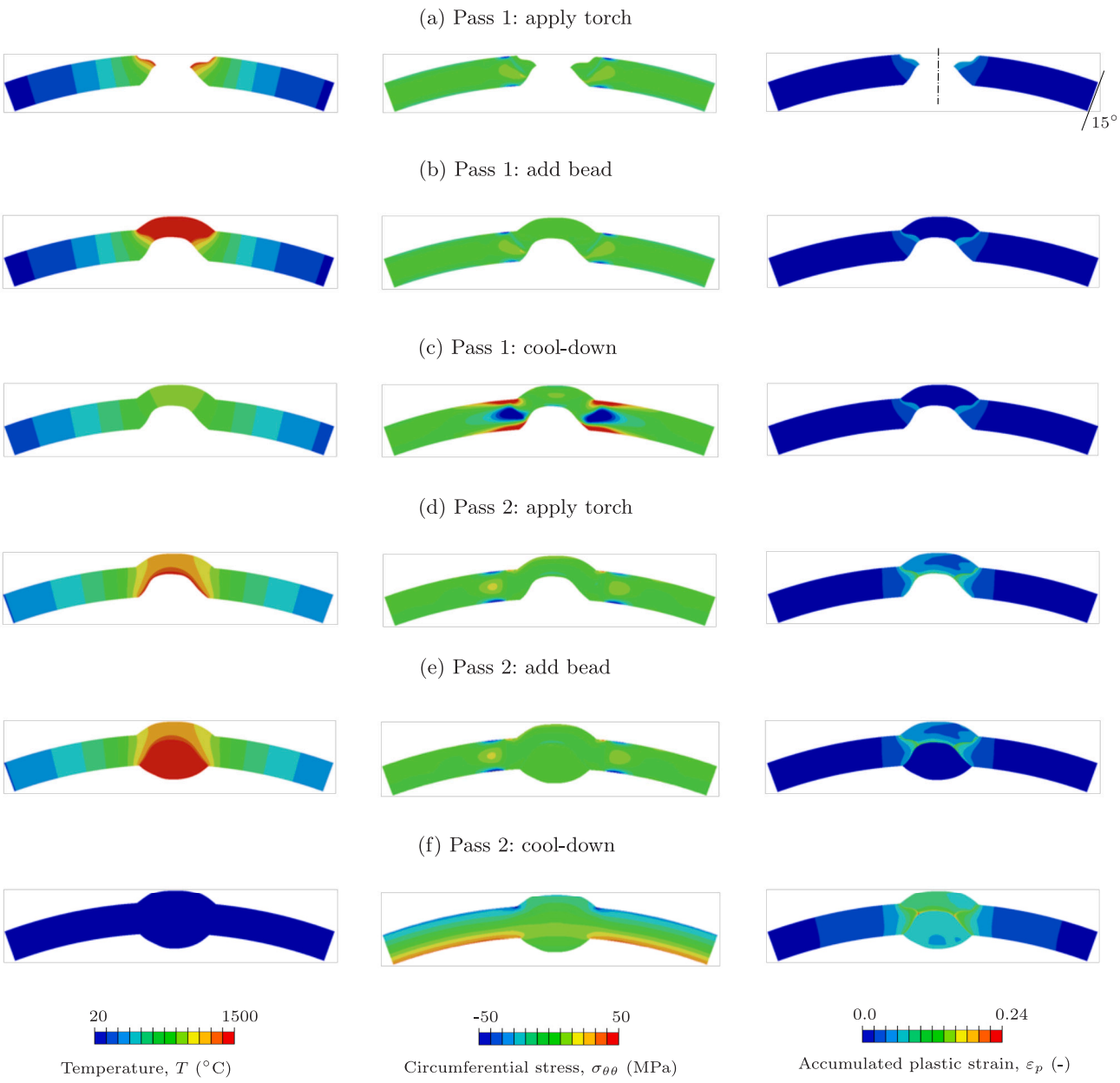

Fig. 6. Evolution of temperature, residual stress and plastic strain in the two-pass welding process. This set of representative results has been obtained for X52 pipeline steel.

which results in yielding pressures of 45 MPa for the X80 pipeline and of 29 MPa for the X52 steel. Despite its intrinsic assumptions, this analytical estimate is not far from the finite element predictions and similar values of yielding pressures are obtained in the numerical calculations if a global yielding criterion such as $\varepsilon_p \geq 0.02$ in the base metal is adopted. Calculations were arrested if cracking had not taken place before the aforementioned critical yielding pressures were reached, ensuring the validity of Eq. (19).

The evolution of stress, plasticity, hydrogen concentration, and phase field fracture are shown in Fig. 7 for the representative case of the X80 welded joint. The initial state (Fig. 7a) is hydrogen-free and shows no damage, but welding residual stresses and plastic strains are present. As the applied pressure increases (Fig. 7b), we observe an increase in circumferential stresses and hydrogen content. The hydrogen distribution varies monotonically from the inner concentration to the $C = 0$ magnitude of the outer surface. The different diffusivities of weld and base material do not appear to have a significant impact on the hydrogen distributions, given the slow loading rate adopted. In this regard, it is worth noting that the magnitude of the residual tensile hydrostatic stress resulting from the welding process is not high enough to accumulate hydrogen within the heat-affected zone (HAZ) under the conditions considered here. As the pressure keeps rising (Fig. 7c), higher stresses and hydrogen concentrations are predicted and this eventually leads to the nucleation of a crack near the weld-base metal junction that goes on to propagate until reaching the outer surface, degrading the load carrying capacity of the pipeline. This crack nucleates at the inner surface of the pipeline section, where the hydrogen content is higher and thus the material toughness is lower. For this weld configuration and material (X80 pipeline steel), cracking takes place at an applied pressure of 31 MPa (i.e., much before yielding). However, X52 is comparatively more ductile and yields before cracking is predicted.

We shall now proceed to investigate the influence of residual stresses, so as to determine the importance of optimising the welding process. Fig. 8 shows the failure predictions obtained for the X80 pipeline steel case for simulations accounting for and neglecting residual stresses. It can be seen that in the absence of residual stresses,

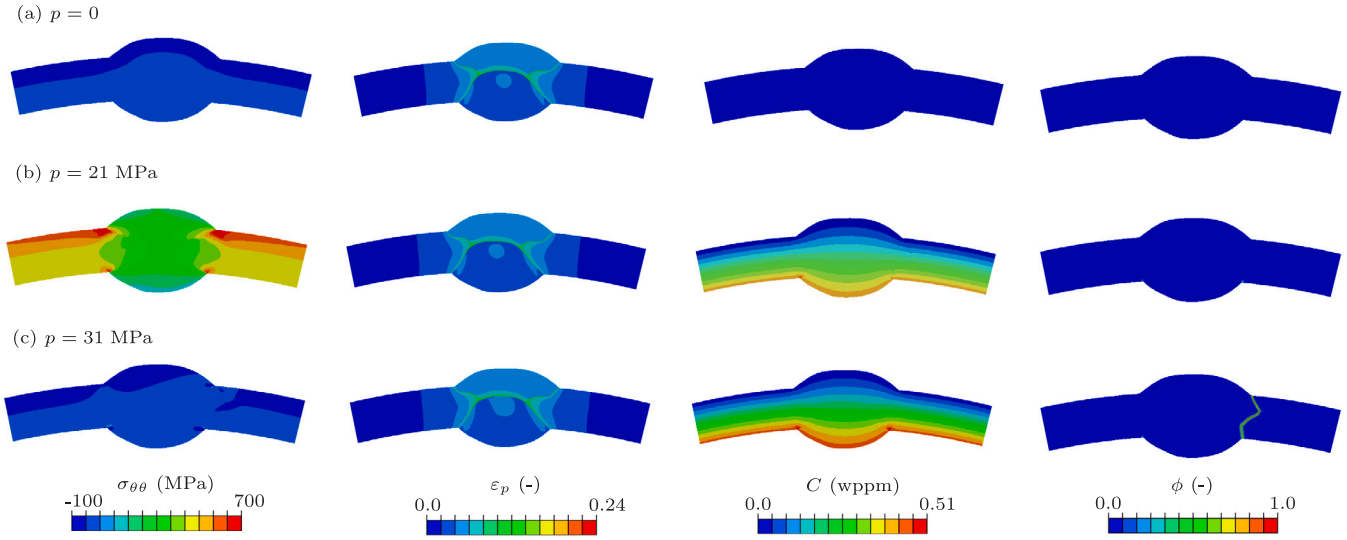

Fig. 7. Predictions of circumferential stress ($\sigma_{\theta\theta}$), accumulated plastic strain (ε_p), lattice hydrogen concentration (C), and phase field fracture (ϕ) as a function of the pipeline pressure: (a) initial state ($p = 0$), (b) $p = 21$ MPa, and (c) $p = 31$ MPa. Results obtained for the two-pass weld considering X80 pipeline steel as the base and weld materials.

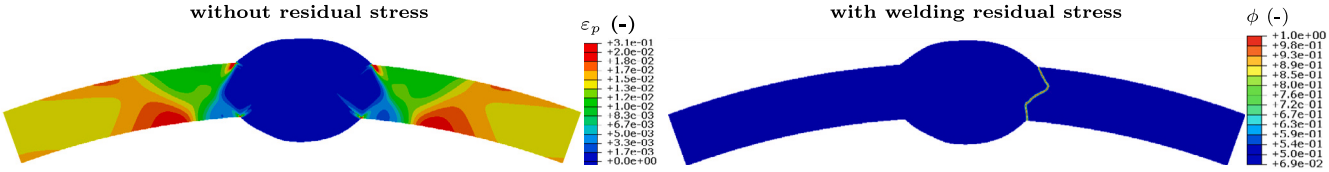

Fig. 8. Investigating the role of welding residual stresses on the failure of hydrogen transport pipelines: in the absence of residual stresses plastic failure occurs (left, ε_p contours), while when residual stresses are accounted for cracking is observed (right, ϕ contours). Results obtained for the two-pass weld considering X80 pipeline steel as the base and weld materials.

the weld pipeline section fails due to yielding, at $p \approx 45$ MPa, while incorporating residual stresses results in cracking at lower pressures ($p \approx 31$ MPa). Hence, the results suggest that weld quality can be of significant importance and that structural integrity predictions must account for the role of welding residual stresses.

Another aspect to consider is the potential presence of voids (pores) that can result from the welding process due to gas trapping. Typical diameters for pores resulting from welding gas trapping are within the range of 4 to 10 μm. Hence, we introduce a random distribution of voids with an approximate size of 7 μm and vary their number to consider various volume fractions, ranging from 0 to 0.5%. The voids are introduced by defining an initial condition of $\phi = 1$ on randomly selected nodes. The results obtained are presented in Fig. 9, showing both the sensitivity of the critical failure pressure to the void volume fraction and the phase field contours, so as to observe cracking patterns and initial void distributions. The results show a change in cracking pattern, with cracks still originating near the inner surface (where the hydrogen content is higher) and next to the weld-base material junction, but with the crack trajectory being influenced by the presence of voids. The critical failure pressure appears to be sensitive to the volume fraction of microvoids, with this trend accelerating for high microvoid volume fractions such that the critical pressure drops from 31 MPa to 24 MPa for a void volume fraction of 0.005. In the case of the X52 pipeline steel case, the presence of voids of 7 μm diameter with volume fractions of 0.005 or smaller does not change the failure mode; the X52 pipeline fails by yielding independently of the presence of voids. This outcome is similar to the fact that the X52 behaviour was not sensitive to welding residual stress.

An important concern when assessing the viability of using the existing natural gas pipeline network to transport hydrogen is the possible presence of existing defects and the role that they can play in lowering the admissible pressures. Internal and near-surface cracks of up to 3–5 mm in length are expected to be present in existing infrastructure. Therefore, we conducted simulations for different pre-existing defect scenarios to assess their impact on performance. As with the pores, these defects were introduced by defining as initial condition $\phi = 1$ on selected nodes. First, the evaluation was carried out on the X80 pipeline steel case. Fig. 10 shows the results obtained in the presence of three 5 mm long internal flaws oriented at 60° relative to the horizontal axis. Two scenarios were considered, one where the flaws were located in the centre region of the weld — roughly equidistant to the inner and outer surfaces (Fig. 10a), and another where the flaws were still internal (not exposed to the surface) but much closer to the inner surface (Fig. 10b). In the former scenario, crack growth occurs from both the top and bottom of the flaw closest to the HAZ resulting in a brittle fracture at a hydrogen pressure of $p_{\max} = 23$ MPa. Cracking was predicted at a pressure of $p_{\max} = 22$ MPa, for the case of the near-surface flaws. The results suggest that the location of the flaw relative to the HAZ is a key factor, more critical than the distance between the flaw and the inner surface, and that the presence of internal defects can reduce the maximum admissible pressure by 20%–30% relative to the defect-free scenario (where $p_{\max} = 31$ MPa, see Fig. 7).

Next, we studied the role of the crack orientation and length on performance. For this, we estimated the critical failure pressure for an existing flaw that was located near the HAZ, at the weld-base material junction, and which was inclined at 60°, 30° and 0° from the horizontal axis. Two crack lengths were considered: 3 and 7 mm. As shown in Fig. 11, the horizontal flaw exhibited a very different cracking pattern relative to the other two scenarios. Although no significant reduction in admissible pressure was predicted ($p_{\max} = 28$ MPa, relative to a defect-free estimate of $p_{\max} = 31$ MPa). However, the 3 mm cracks aligned closer to the HAZ appear to have a very significant impact on the pressure-carrying capacity. We find that pipeline failure occurs at

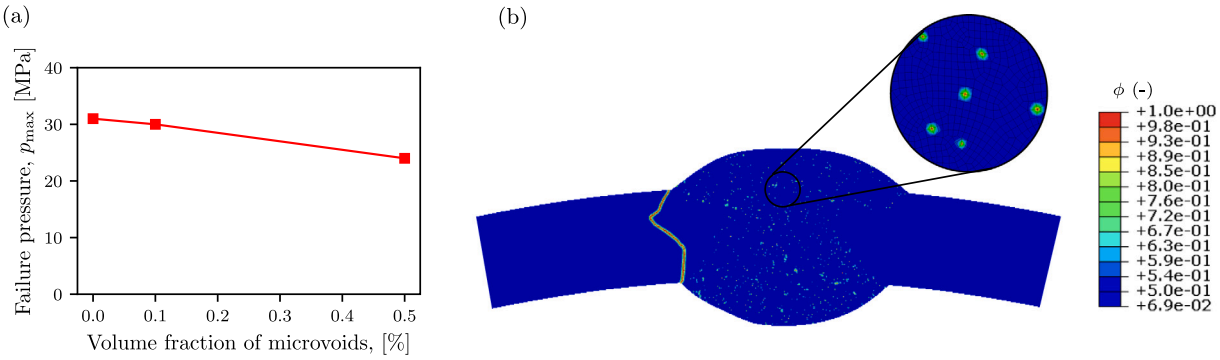

Fig. 9. Investigating the role of porosity on the failure of hydrogen transport pipelines: (a) sensitivity of the critical failure pressure to the void volume fraction, and (b) cracking pattern (phase field contours) observed for a volume fraction of 0.5%, which corresponds to a critical pressure of p_{max} = 24 MPa. Results obtained for the two-pass weld considering X80 pipeline steel as the base and weld materials.

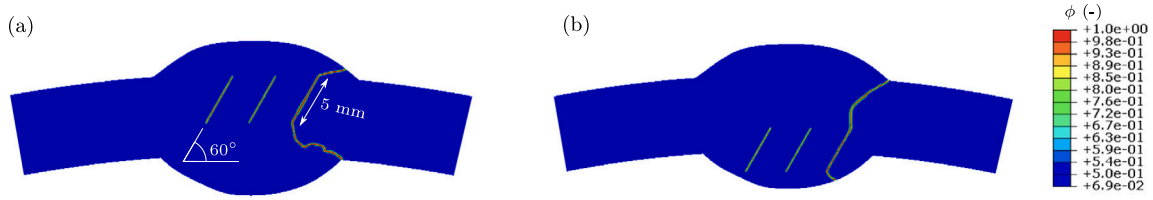

Fig. 10. Investigating the role of internal pre-existing defects on the failure of hydrogen transport pipelines. Phase field contours for three internal flaws aligned 60° relative to the horizontal direction under two scenarios: (a) located near the centre of the pipeline section (p_{max} = 23 MPa), and (b) located near the inner surface (p_{max} = 22 MPa). Results obtained for the two-pass weld considering X80 pipeline steel as the base and weld materials.

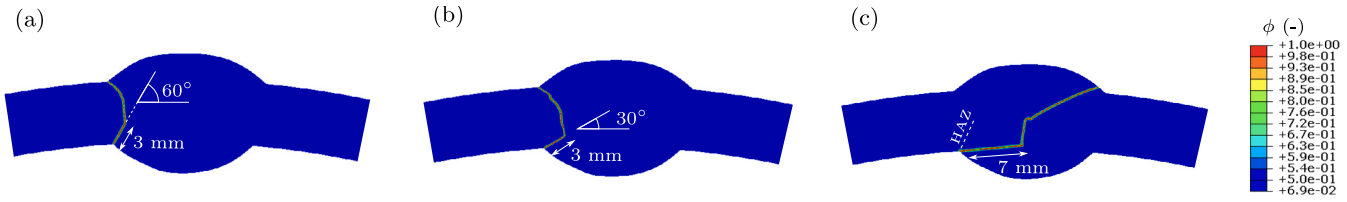

Fig. 11. Investigating the role of external pre-existing defects on the failure of hydrogen transport pipelines. An initial flaw is assumed to be present at the weld-base material junction, near the HAZ region, and the influence of crack length and orientation (relative to the horizontal axis) is assessed by considering: (a) a 3 mm flaw with 60° orientation (p_{max} = 15 MPa), (b) a 3 mm flaw with 30° orientation (p_{max} = 19 MPa), and (c) a 7 mm flaw with 0° orientation (p_{max} = 28 MPa). Results obtained for the two-pass weld considering X80 pipeline steel as the base and weld materials.

p_{max} = 19 MPa, for the 30° orientation, and at p_{max} = 15 MPa, for the 60° orientation.

Thus, defect location appears to play a critical role in fracture behaviour. Failure pressures of 15 MPa are of significant technological importance as they lie within the ranges considered for hydrogen transport. Furthermore, while this drop in load-carrying capacity is attained under specific conditions, these scenarios were selected to be relevant to existing pipelines. Indeed, defects of similar size and location have been reported on seam welds of gas transport pipelines and is expected that defects will originate near the inner surface and along the harder and more brittle HAZ region. When a similar analysis was conducted on the more ductile X52 pipeline steel, a change in failure mode from global yielding to cracking was observed. The predicted critical failure pressure dropped to p_{max} = 18 MPa when a 3 mm flaw was present along the HAZ — see Fig. 12.

3.2. Case study 2: three-pass seam weld

A second seam weld configuration is investigated to assess the role of weld quality and geometry on performance. The second weld also facilitated the investigation of the influence of weld microstructural heterogeneity. As shown in Fig. 4b, we considered a seam weld fabricated using three-passes. The overall weld dimensions were 21 × 13 mm. Microhardness mapping had been performed on this ex-service weld. This weld configuration is representative of seam welds that require a third, repair weld pass. The material properties adopted are largely those reported in Table 3 but some changes are introduced to incorporate the information provided by the microstructural hardness map. Namely, the ASTM-A370 relationship is adopted to quantitatively relate the HV measurements with yield strength, with σ_y varying between 660 and 990 MPa for the X80 pipeline steel and between 430 and 645 MPa for the X52 pipeline steel (see Fig. 13). The fracture-to-yield strength ratio was maintained at the previous level, and this brings a variation in the fracture strength ($\hat{\sigma}$) distribution, as shown in Fig. 13. Also, since a higher strength typically corresponds to a lower toughness, the analysis performed considered that the fracture energy varied inversely to the microhardness. Finally, and consistent with experimental observations [78], the diffusivity was assumed to be lower in hard regions. The other parameters were kept the same as in Table 3, with Poisson's ratio and strain hardening exponent being uniform across the section (ν = 0.3 and n = 0.1, respectively). As observed in Fig. 13, this microstructural mapping allows the variations in strength and toughness of the HAZ regions to be displayed.

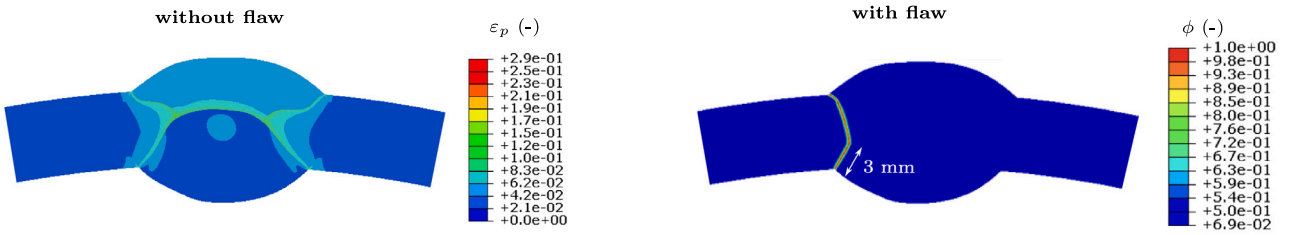

Fig. 12. Investigating the role of an external pre-existing flaw that is located near the inner surface and aligned with the HAZ. Results obtained for the two-pass weld considering X52 pipeline steel as the base and weld materials. The finite element analysis reveals: a global yielding type of failure at $p_{max} \approx 29$ MPa) in the absence of flaws (a), yet a brittle fracture event at a pressure of $p_{max} = 19$ MPa in the presence of a 3 mm flaw along the HAZ (b).

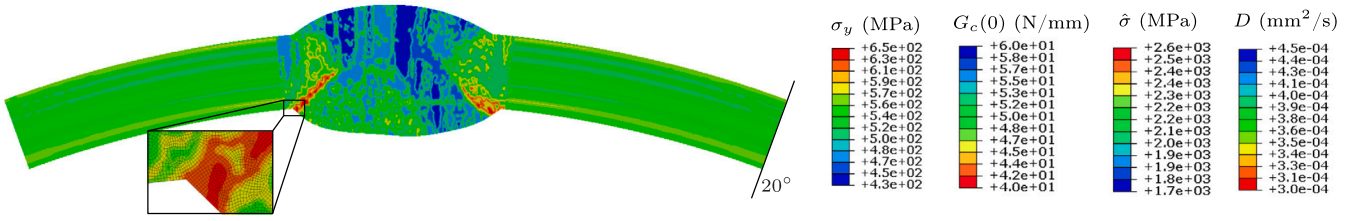

Fig. 13. Spatial distribution of relevant material properties (yield stress, toughness, strength and diffusivity) as inferred from the microhardness map of the three-pass weld (see Fig. 4). The results shown correspond to the X52 pipeline steel case.

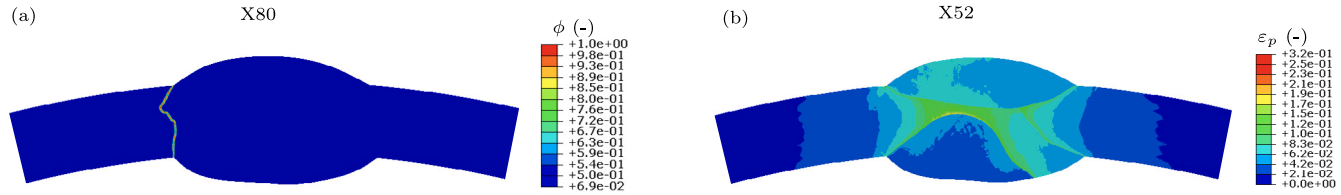

Fig. 14. Computational predictions of weld structural integrity in hydrogen transport pipelines: (a) brittle fracture in an X80 pipeline at a critical pressure of $p_{max} = 24$ MPa, (b) failure by global plastic yielding in an X52 pipeline.

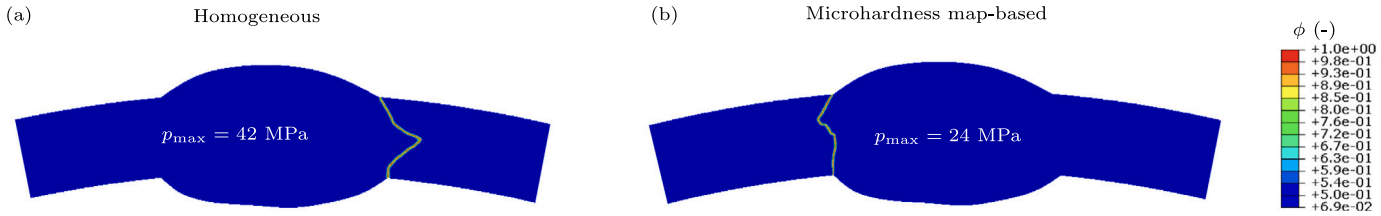

Fig. 15. Investigating the role of accounting for the microstructural heterogeneity of seam welds. Cracking (phase field) contours for: (a) the case where material properties are considered to be homogeneous in the weld and base metal regions, and (b) the case where material properties are varied according to the microstructural hardness map (see Figs. 4 and 13). Failure takes place due to cracking at critical pressures of $p_{max} = 42$ MPa and $p_{max} = 24$ MPa, respectively.

As in the previous case study, a two-step analysis was conducted. This started with a welding process simulation to obtain the associated residual stresses, and was followed by a coupled deformation–diffusion–fracture analysis to determine the maximum admissible pressure. The evolution of the stress fields, the equivalent plastic distribution and the phase field fracture variability in this welded joint was qualitatively similar to that of the previous weld geometry despite the differences in the welding process and the heterogeneous distribution of material properties. However, interesting differences were found when inspecting the critical failure pressures and the cracking patterns. First, as shown in Fig. 14, the X80 pipeline was predicted to fail due to cracking at a pressure of $p_{max} = 24$ MPa, a lower magnitude than that reported for the two-pass weld in the absence of defects (31 MPa). The cracking pattern was also slightly different, with the crack nucleating at the intersection between the HAZ and the inner surface but growing mostly through the base metal. In contrast, the X52 pipeline was predicted to fail due to global plastic yielding, as observed in the two-pass weld.

Calculations were also conducted with homogeneous material properties, as in the two-pass weld case study, to quantify the influence of the inherent microstructural heterogeneity of welded components. The results, shown in Fig. 15, reveal a notable influence of the material microstructure. When the material properties were taken to be homogeneous in the base metal and the weld, then failure was predicted to take place at a pressure of $p_{max} = 42$ MPa. However, when the microstructural heterogeneity of the material was accounted for, the predicted fracture pressure was reduced by approximately 50%, to $p_{max} = 24$ MPa. Interestingly, the failure pressure obtained for the homogeneous case study is significantly higher than that reported for the 17 × 14 mm two-pass weld under the same conditions (31 MPa). This suggests that the three-pass weld with dimensions 21 × 13 mm is more resistant to hydrogen-assisted fractures. This also

suggests that the lower bound of p_{max} = 15 MPa obtained for the two-pass weld in the presence of a HAZ-aligned 3 mm flaw could be further reduced if microstructural heterogeneities are accounted for.

4. Conclusions

We have presented a computational framework for predicting the maximum admissible pressure in hydrogen transport pipelines. The framework combines welding process modelling, to determine the residual stress state, with coupled deformation–diffusion–fracture (embrittlement) simulations, to quantify critical fracture pressures. The focus is on maximising simplicity and predictive abilities. As such, the model relies only on parameters with a clear physical interpretation, that can be independently measured. Virtual experiments were conducted on pipelines containing two types of seam welds. These were selected to represent real welds in gas transport pipelines: a two-pass weld of dimensions 17 × 14 mm, and a three-pass weld of dimensions 21 × 13 mm, for which a microstructural hardness map exists. The model was first benchmarked against crack growth resistance curves on X52 and X80 pipeline steels. Then the model was used to investigate the influence of residual stresses, welding quality and geometry, microstructure, internal and external defects, and hydrogen gas pressure. Key findings include:

- An accurate characterisation of residual stresses can be decisive in determining the failure mode. In the absence of pre-existing defects, X80 pipeline steels were predicted to fail by global plastic yielding (at $p_{max} \approx 45$ MPa) if residual stresses are neglected. However, cracks are found to nucleate and grow across the pipeline cross-section at 31 MPa H_2 pressures when the impact of residual stresses arising from the welding process was taken into account.
- The presence of micrometer pores with volume fractions below 0.005 can reduce the admissible pressure in X80 pipelines to $p_{max} = 24$ MPa. The presence of pores was not predicted to play a role in the performance of the more ductile X52 pipelines, which fail by global plastic yielding (in the absence of other defects).
- The maximum admissible pressure was found to be very sensitive to the size, location and orientation of pre-existing defects. Those closer to the inner surface of the pipeline (where the hydrogen content is greater) and aligned with and near to the HAZ being the most harmful.
- The presence of 3 mm long surface flaws which are aligned with the HAZ can significantly reduce the pressure-carrying capacity of hydrogen transport pipelines. This realistic scenario results in a maximum admissible pressure of p_{max} = 15 MPa for the X80 pipelines and of $p_{max} = 19$ MPa for the X52 pipeline.
- The weld geometry and quality were found to be important. This highlights the need to characterise the welds of the existing natural gas pipeline infrastructure and to ensure that best practice is used when manufacturing new welds.
- The microstructural heterogeneity of the weld region is found to play a key role, potentially changing the critical failure pressure by approximately 50% relative to the consideration of homogeneous weld and base materials.

These findings and the computational tools developed are expected to be of significant importance to the potential deployment of a hydrogen transport pipeline network, given the challenges associated with laboratory and field assessment.

Multiple avenues of future work can be envisaged. First, significant work is ongoing in the weld process modelling community to develop more sophisticated descriptions of residual stresses and microstructural phases. One could build upon such modelling efforts not only to provide a more detailed description but also to validate with experimental testing (e.g., by comparing real and virtual hardness maps). In addition, other aspects of the deformation–diffusion–fracture modelling could be readily incorporated, if deemed relevant, from fatigue damage to explicit consideration of trapping sites.

Declaration of competing interest

The authors declare that they have no known competing financial interests or personal relationships that could have appeared to influence the work reported in this paper.

Acknowledgements

The authors acknowledge financial support from EPRI through the R&D project "*Virtual Testing* of hydrogen-sensitive components". E. Martínez-Pañeda additionally acknowledges financial support from UKRI's Future Leaders Fellowship programme [grant MR/V024124/1]. T. K. Mandal gratefully acknowledges stimulating discussions on phase field modelling, image processing, and weld simulation with Adria Quintanas-Corominas (Barcelona Supercomputing Center, Spain), Abhinav Gupta (Vanderbilt University, USA), Yousef Navidtehrani (University of Oviedo, Spain) and Lucas Castro García (University of Oviedo, Spain).

Appendix. Model verification: crack growth resistance curves

Here, we showcase the ability of the model to predict the crack growth resistance of pipeline steels and rationalise the values of the fracture parameters chosen in this study. For a set of given elastoplastic material properties, the crack growth resistance (R-curve) behaviour is primarily governed by the fracture energy G_c and fracture strength $\hat{\sigma}$ of the material [80,81]. In the phase field model here adopted, the former is explicitly provided, as G_c is an input variable, while the latter is defined through the choice of phase field length scale, as per Eq. (12). It should be noted that for boundary value problems with sufficiently large cracks (longer than the transition flaw size), the fracture behaviour is toughness-dominated and crack growth is therefore governed by G_c and independent of the fracture strength. However, $\hat{\sigma}$ does influence the amount of dissipation during subcritical crack growth [80,81], and thus should be chosen appropriately. This R-curve modelling exercise allows for this. Another aspect to note is that while the $G \equiv J$ analogy holds, the critical value of the energy release rate in the phase field model, G_c, does not correspond to J_{Ic}, as the latter is measured after 0.2 mm of crack extension while G_c corresponds to the onset of crack growth. As such, the measured J_{Ic} value provides only one data point and the entire R-curve is needed to ensure that the model provides an accurate characterisation of crack growth resistance. An appropriate set of $(G_c, \hat{\sigma})$ values has to be determined, through appropriate choices of G_c and ℓ. In this regard, it should be noted that measuring G_c (also referred to as J_0) is not straightforward, given the challenges associated with capturing the onset of crack growth (particularly in hydrogen-containing environments).

Crack growth resistance curves are obtained by making use of the so-called boundary layer formulation, whereby William's solution [82] for a remote elastic K-field is used to prescribe the displacement of the outer nodes (see Fig. A.1). Accordingly, the displacement field is given by,

$$u_i = \frac{K_I}{E} r^{1/2} f_i(\theta, \nu), \tag{A.1}$$

where r and θ are the coordinates of a polar coordinate system centred at the crack tip and K_I is the mode I stress intensity factor, which under small scale yielding conditions is related to the J-integral as $J_I = K_I^2(1-\nu^2)/E$. As per William's solution [82], the function f_i reads,

$$f_x = \frac{1+\nu}{\sqrt{2\pi}}\left(3-4\nu-\cos\theta\right)\cos\left(\frac{\theta}{2}\right), \quad f_y = \frac{1+\nu}{\sqrt{2\pi}}\left(3-4\nu-\cos\theta\right)\sin\left(\frac{\theta}{2}\right). \tag{A.2}$$

We take advantage of the reflective symmetry of the boundary value problem about the crack plane and simulate only half of the complete

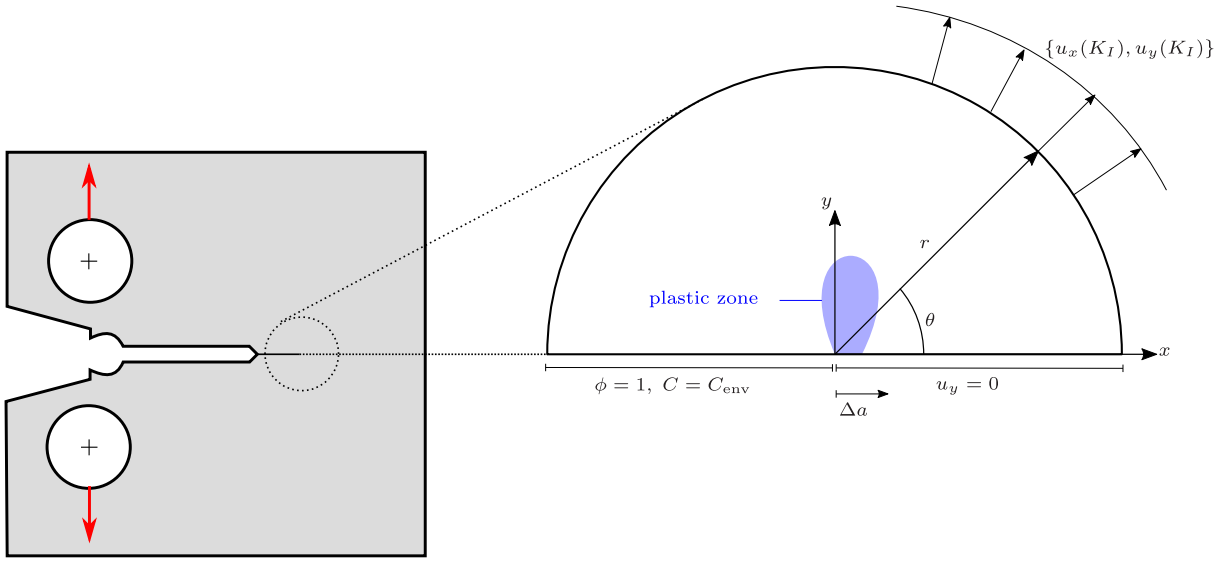

Fig. A.1. The boundary layer idealisation of a compact tension specimen under small-scale yield conditions. R-curves are obtained by applying a remote K (J) and measuring the crack extension Δa.

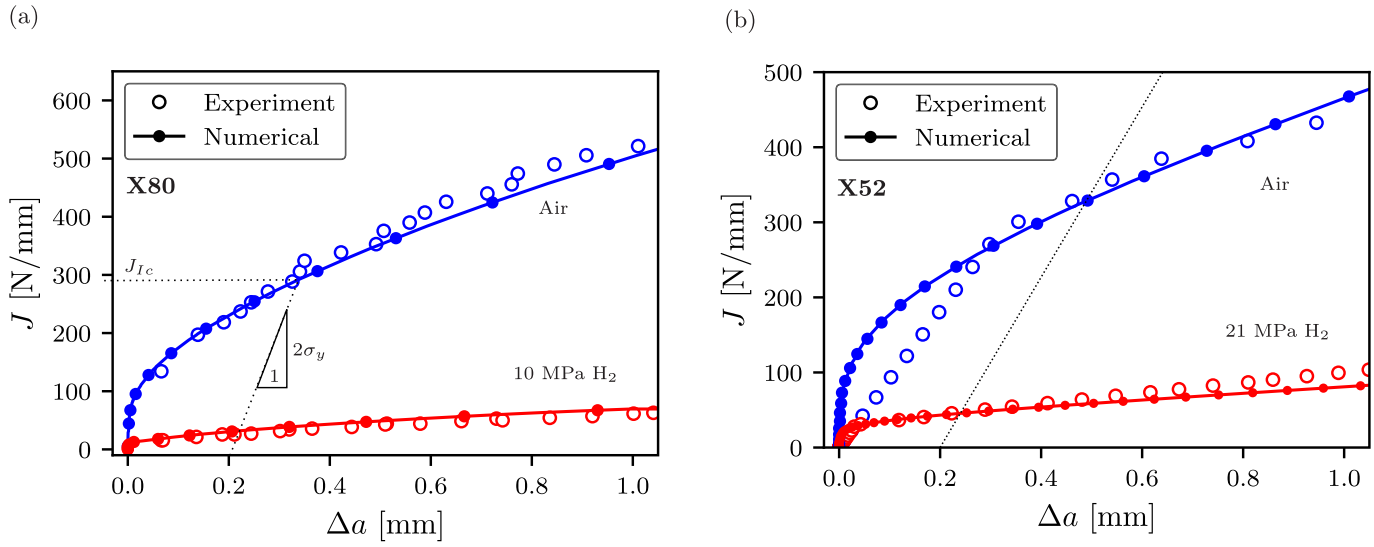

Fig. A.2. Predicting the crack growth resistance behaviour of (a) X80 pipeline steel [66], and (b) X52 pipeline steel [63], in both air and hydrogen environments.

boundary layer, as shown in Fig. A.1. The outer radius is chosen to be sufficiently large so as to not influence the results: $R \gg R_p$, with R_p being Irwin's estimate of the plastic zone length,

$$R_p := \frac{1}{3\pi}\frac{K_I}{\sigma_y^2}. \tag{A.3}$$

In all calculations, the characteristic element size is taken to be five times smaller than the phase field length scale, so as to ensure mesh objective results [83]. The material properties for X80 and X52 pipeline steels are taken from the literature, and are consistent with the base metal parameters reported in the main text. Namely, the elastic properties are taken to be $E = 187$ GPa and $\nu = 0.3$ [66], and the fit of the hardening law adopted to the uniaxial stress–strain data from Ref. [84] renders a hardening exponent of $n = 0.1$. The values of yield stress are $\sigma_y = 660$ MPa and $\sigma_y = 430$ MPa for, respectively, X80 and X52 pipeline steel (Table 2). The numerical experiments mimic the conditions of the laboratory tests used as a benchmark (see Refs. [63,66]). The hydrogen concentration corresponding to the reported H_2 pressure is determined using Sievert's law (Eq. (18)). Also, as in the experiments, a very slow loading rate ($\dot{K}_I \sim 0.05$ MPa $\sqrt{\text{m}}$ /s) is adopted. The results obtained are shown in Fig. A.2.

As shown in Fig. A.2, for both X80 and X52 pipeline steels, the chosen values $G_c(0)$ and $\hat{\sigma}$ deliver a very good agreement with experimental measurements. These values are provided in Table A.1 and are subsequently used to predict the behaviour of welded components exposed to hydrogen environments (see Section 3). It is important to note that hydrogen affects not only the load at which cracking initiates but also the slope of the R-curve, diminishing the degree of plastic dissipation. Hence, the hydrogen degradation law estimated from J_{Ic} vs. C (or p) data is not necessarily the same as that describing the sensitivity of G_c (or J_0) to C; i.e.,

$$\frac{G_c(C)}{J_{Ic}(C)} = d(C)\frac{G_c(0)}{J_{Ic}(0)} \tag{A.4}$$

where $d(C) \geq 1$ is a variable that characterises the higher degree of hydrogen degradation experienced by J_{Ic} relative to G_c (or J_0), as a

Table A.1
Calibrated phase field model parameters for pipeline steels.

Steel	σ_y [MPa]	$G_c(0)$ [N/mm]	$G_c^{\min}$ [N/mm]	$\hat{\sigma}/\sigma_y$ [–]
X80	660	60	7	4
X52	430	60	16	4

result of the hindered plastic dissipation. Accordingly, Eq. (17) can be re-written as,

$$G_c(C) = f(C)d(C)G_c(0) = \left[\frac{G_c^{\min}}{G_c(0)} + \left(1 - \frac{G_c^{\min}}{G_c(0)}\right)\exp\left(-q_1 C^{q_2}\right)\right] G_c(0). \tag{A.5}$$

References

[1] Lipiäinen S, Lipiäinen K, Ahola A, Vakkilainen E. Use of existing gas infrastructure in European hydrogen economy. Int J Hydrogen Energy 2023;48(80):31317–29.
[2] Thawani B, Hazael R, Critchley R. Assessing the pressure losses during hydrogen transport in the current natural gas infrastructure using numerical modelling. Int J Hydrogen Energy 2023;48:34463–75.
[3] Laureys A, Depraetere R, Cauwels M, Depover T, Hertelé S, Verbeken K. Use of existing steel pipeline infrastructure for gaseous hydrogen storage and transport: A review of factors affecting hydrogen induced degradation. J Nat Gas Sci Eng 2022;101:104534.
[4] Galyas AB, Kis L, Tihanyi L, Szunyog I, Vadaszi M, Koncz A. Effect of hydrogen blending on the energy capacity of natural gas transmission networks. Int J Hydrogen Energy 2023;48(39):14795–807.
[5] Penev M, Zuboy J, Hunter C. Economic analysis of a high-pressure urban pipeline concept (HyLine) for delivering hydrogen to retail fueling stations. Transp Res D 2019;77:92–105.
[6] Rong Y, Chen S, Li C, Chen X, Xie L, Chen J, Long R. Techno-economic analysis of hydrogen storage and transportation from hydrogen plant to terminal refueling station. Int J Hydrogen Energy 2023;52:547–58.
[7] Gangloff RP. Hydrogen-assisted cracking. In: Milne I, Ritchie R, Karihaloo B, editors. Comprehensive structural integrity. Vol. 6, New York, NY: Elsevier Science; 2003, p. 31–101.
[8] Gangloff RP, Somerday BP. Gaseous hydrogen embrittlement of materials in energy technologies. Cambridge: Woodhead Publishing Limited; 2012.
[9] Djukic MB, Bakic GM, Sijacki Zeravcic V, Sedmak A, Rajicic B. The synergistic action and interplay of hydrogen embrittlement mechanisms in steels and iron: Localized plasticity and decohesion. Eng Fract Mech 2019;216:106528.
[10] San Marchi CW, Somerday BP. Technical reference for hydrogen compatibility of materials. Tech. rep., Albuquerque, NM, and Livermore, CA: Sandia National Laboratories (SNL); 2012.
[11] Boukortt H, Amara M, Hadj Meliani M, Bouledroua O, Muthanna B, Suleiman R, Sorour A, Pluvinage G. Hydrogen embrittlement effect on the structural integrity of API 5L X52 steel pipeline. Int J Hydrogen Energy 2018;43(42):19615–24.
[12] Briottet L, Ez-Zaki H. Influence of hydrogen and oxygen impurity content in a natural gas / hydrogen blend on the toughness of an API X70 steel. In: ASME 2018 pressure vessels and piping conference. American Society of Mechanical Engineers Digital Collection; 2018, p. 1–5.
[13] Ronevich J, Agnani M, Marchi CS. Effects of testing rate on hydrogen-assisted fracture of ferritic steels. In: International conference on fracture. ICF15, Atlanta, USA; 2023, p. 1–2.
[14] Ronevich JA, Somerday BP, Feng Z. Hydrogen accelerated fatigue crack growth of friction stir welded X52 steel pipe. Int J Hydrogen Energy 2017;42(7):4259–68.
[15] Ronevich JA, Song EJ, Feng Z, Wang Y, D'Elia C, Hill MR. Fatigue crack growth rates in high pressure hydrogen gas for multiple X100 pipeline welds accounting for crack location and residual stress. Eng Fract Mech 2020;228:106846.
[16] Song EJ, Baek S-W, Nahm SH, Baek UB. Notched-tensile properties under high-pressure gaseous hydrogen: Comparison of pipeline steel X70 and austenitic stainless type 304L, 316L steels. Int J Hydrogen Energy 2017;42(12):8075–82.
[17] Meng B, Gu C, Zhang L, Zhou C, Li X, Zhao Y, Zheng J, Chen X, Han Y. Hydrogen effects on X80 pipeline steel in high-pressure natural gas/hydrogen mixtures. Int J Hydrogen Energy 2017;42(11):7404–12.
[18] Ishikawa N, Sakimoto T, Shimamura J, Wang J, Wang Y-Y. Integrity assessment of linepipes for transporting high pressure hydrogen based on ASME B31.12. In: 2022 14th international pipeline conference. American Society of Mechanical Engineers Digital Collection; 2022, p. 1–9.
[19] Kappes MA, Perez TE. Blending hydrogen in existing natural gas pipelines: Integrity consequences from a fitness for service perspective. J Pipeline Sci Eng 2023;100141.
[20] Martínez-Pañeda E. Progress and opportunities in modelling environmentally assisted cracking. RILEM Tech Lett 2021;6:70–7.
[21] Cheng G, Wang X, Chen K, Zhang Y, Venkatesh TA, Wang X, Li Z, Yang J. Probing the effects of hydrogen on the materials used for large-scale transport of hydrogen through multi-scale simulations. Renew Sustain Energy Rev 2023;182(September 2022):113353.
[22] Martínez-Pañeda E, Díaz A, Wright L, Turnbull A. Generalised boundary conditions for hydrogen transport at crack tips. Corros Sci 2020;173:108698.
[23] Hageman T, Martínez-Pañeda E. An electro-chemo-mechanical framework for predicting hydrogen uptake in metals due to aqueous electrolytes. Corros Sci 2022;208:110681.
[24] Sofronis P, McMeeking RM. Numerical analysis of hydrogen transport near a blunting crack tip. J Mech Phys Solids 1989;37(3):317–50.
[25] Martínez-Pañeda E, del Busto S, Niordson CF, Betegón C. Strain gradient plasticity modeling of hydrogen diffusion to the crack tip. Int J Hydrogen Energy 2016;41(24):10265–74.
[26] Dadfarnia M, Sofronis P, Neeraj T. Hydrogen interaction with multiple traps: Can it be used to mitigate embrittlement? Int J Hydrogen Energy 2011;36(16):10141–8.
[27] Fernández-Sousa R, Betegón C, Martínez-Pañeda E. Analysis of the influence of microstructural traps on hydrogen assisted fatigue. Acta Mater 2020;199:253–63.
[28] Isfandbod M, Martínez-Pañeda E. A mechanism-based multi-trap phase field model for hydrogen assisted fracture. Int J Plast 2021;144:103044.
[29] Cupertino Malheiros L, Oudriss A, Cohendoz S, Bouhattate J, Thébault F, Piette M, Feaugas X. Local fracture criterion for quasi-cleavage hydrogen-assisted cracking of tempered martensitic steels. Mater Sci Eng A 2022;847:143213.
[30] Valverde-González A, Martínez-Pañeda E, Quintanas-Corominas A, Reinoso J, Paggi M. Computational modelling of hydrogen assisted fracture in polycrystalline materials. Int J Hydrogen Energy 2022;47(75):32235–51.
[31] Serebrinsky S, Carter EA, Ortiz M. A quantum-mechanically informed continuum model of hydrogen embrittlement. J Mech Phys Solids 2004;52(10):2403–30.
[32] Moriconi C, Hénaff G, Halm D. Cohesive zone modeling of fatigue crack propagation assisted by gaseous hydrogen in metals. Int J Fatigue 2014;68:56–66.
[33] del Busto S, Betegón C, Martínez-Pañeda E. A cohesive zone framework for environmentally assisted fatigue. Eng Fract Mech 2017;185:210–26.
[34] Elmukashfi E, Tarleton E, Cocks ACF. A modelling framework for coupled hydrogen diffusion and mechanical behaviour of engineering components. Comput Mech 2020;66:189–220.
[35] Colombo C, Zafra García A, Belzunce J, Fernandez Pariente I. Sensitivity to hydrogen embrittlement of AISI 4140 steel: A numerical study on fracture toughness. Theor Appl Fract Mech 2020;110:102810.
[36] Dadfarnia M, Somerday BP, Schembri PE, Sofronis P, Foulk JW, Nibur KA, Balch DK. On modeling hydrogen-induced crack propagation under sustained load. JOM 2014;66(8):1390–8.
[37] Anand L, Mao Y, Talamini B. On modeling fracture of ferritic steels due to hydrogen embrittlement. J Mech Phys Solids 2019;122:280–314.
[38] Yu H, Olsen JS, Alvaro A, Qiao L, He J, Zhang Z. Hydrogen informed gurson model for hydrogen embrittlement simulation. Eng Fract Mech 2019;217:106542.
[39] Depraetere R, De Waele W, Hertelé S. Fully-coupled continuum damage model for simulation of plasticity dominated hydrogen embrittlement mechanisms. Comput Mater Sci 2021;200:110857.
[40] Martínez-Pañeda E, Golahmar A, Niordson CF. A phase field formulation for hydrogen assisted cracking. Comput Methods Appl Mech Engrg 2018;342:742–61.
[41] Duda FP, Ciarbonetti A, Toro S, Huespe AE. A phase-field model for solute-assisted brittle fracture in elastic–plastic solids. Int J Plast 2018;102:16–40.
[42] Huang C, Gao X. Phase field modeling of hydrogen embrittlement. Int J Hydrogen Energy 2020;45(38):20053–68.
[43] Wu J-Y, Mandal TK, Nguyen VP. A phase-field regularized cohesive zone model for hydrogen assisted cracking. Comput Methods Appl Mech Engrg 2020;358:112614.
[44] Golahmar A, Kristensen PK, Niordson CF, Martínez-Pañeda E. A phase field model for hydrogen-assisted fatigue. Int J Fatigue 2022;154:106521.
[45] Dinachandra M, Alankar A. Adaptive finite element modeling of phase-field fracture driven by hydrogen embrittlement. Comput Methods Appl Mech Engrg 2022;391:114509.
[46] Kristensen PK, Niordson CF, Martínez-Pañeda E. Applications of phase field fracture in modelling hydrogen assisted failures. Theor Appl Fract Mech 2020;110:102837.
[47] Simo JC, Hughes TJ. Computational inelasticity. Vol. 7, Springer Science & Business Media; 1998.
[48] ASME Section II Part D. ASME boiler and pressure vessel code. Three Park Avenue, NY: ASME Boiler and Pressure Vessel Committee on Materials; 2010.
[49] Griffith AA. The phenomena of rupture and flow in solids. Philos Trans R Soc Lond A Math Phys Eng Sci 1920;221:163.
[50] Alvaro A, Thue Jensen I, Kheradmand N, Løvvik OM, Olden V. Hydrogen embrittlement in nickel, visited by first principles modeling, cohesive zone simulation and nanomechanical testing. Int J Hydrogen Energy 2015;40(47):16892–900.
[51] Francfort GA, Marigo J-J. Revisiting brittle fracture as an energy minimization problem. J Mech Phys Solids 1998;46(8):1319–42.

[52] Rabczuk T. Computational methods for fracture in brittle and quasi-brittle solids: State-of-the-art review and future perspectives. ISRN Appl Math 2013.
[53] Bourdin B, Francfort GA, Marigo J-J. Numerical experiments in revisited brittle fracture. J Mech Phys Solids 2000;48(4):797–826.
[54] Miehe C, Welschinger F, Hofacker M. Thermodynamically consistent phase-field models of fracture: Variational principles and multi-field FE implementations. Internat J Numer Methods Engrg 2010;83(10):1273–311.
[55] Chambolle A. An approximation result for special functions with bounded deformation. J Math Pures Appl 2004;83(7):929–54.
[56] Taylor GI, Quinney H. The latent energy remaining in a metal after cold working. Proc R Soc Lond Ser A Math Phys Eng Sci 1933;143(849):307–26.
[57] Amor H, Marigo JJ, Maurini C. Regularized formulation of the variational brittle fracture with unilateral contact: Numerical experiments. J Mech Phys Solids 2009;57(8):1209–29.
[58] Ambati M, Kruse R, De Lorenzis L. A phase-field model for ductile fracture at finite strains and its experimental verification. Comput Mech 2016;57(1):149–67.
[59] Miehe C, Hofacker M, Welschinger F. A phase field model for rate-independent crack propagation: Robust algorithmic implementation based on operator splits. Comput Methods Appl Mech Engrg 2010;199(45–48):2765–78.
[60] Kristensen PK, Niordson CF, Martínez-Pañeda E. An assessment of phase field fracture: crack initiation and growth. Phil Trans R Soc A 2021;379:20210021.
[61] Díaz A, Alegre JM, Cuesta II, Martínez-Pañeda E. A comsol framework for predicting hydrogen embrittlement - part ii: phase field fracture. 2024, (in preparation).
[62] Martínez-Pañeda E, Harris Z, Fuentes-Alonso S, Scully JR, Burns JT. On the suitability of slow strain rate tensile testing for assessing hydrogen embrittlement susceptibility. Corros Sci 2020;163:108291.
[63] Ronevich JA, Song EJ, Somerday BP, San Marchi CW. Hydrogen-assisted fracture resistance of pipeline welds in gaseous hydrogen. Int J Hydrogen Energy 2021;46(10):7601–14.
[64] Ronevich JA, San Marchi C. Materials compatibility concerns for hydrogen blended into natural gas. In: ASME 2021 pressure vessels & piping conference. American Society of Mechanical Engineers Digital Collection; 2021, p. 1–6.
[65] San Marchi C, Ronevich J, Simmons K. Materials evaluation for hydrogen service. Tech. rep. SAND2021-10712PE, Albuquerque, NM (United States), SNL California: Sandia National Lab. (SNL-NM), Sandia National Laboratories; 2021.
[66] Shang J, Wang JZ, Chen WF, Wei HT, Zheng JY, Hua ZL, Zhang L, Gu CH. Different effects of pure hydrogen vs. hydrogen/natural gas mixture on fracture toughness degradation of two carbon steels. Mater Lett 2021;296:129924.
[67] San Marchi C, Somerday BP, Nibur KA, Stalheim DG, Boggess T, Jansto S. Fracture and fatigue of commercial grade API pipeline steels in gaseous hydrogen. In: ASME 2010 pressure vessels and piping division/K-PVP conference. American Society of Mechanical Engineers Digital Collection; 2011, p. 939–48.
[68] San Marchi C, Somerday BP, Nibur KA, Stalheim DG, Boggess T, Jansto S. Fracture resistance and fatigue crack growth of X80 pipeline steel in gaseous hydrogen. In: ASME 2011 pressure vessels and piping conference. American Society of Mechanical Engineers Digital Collection; 2012, p. 841–9.
[69] San Marchi C, Shrestha R, Ronevich J. Hydrogen compatibility of structural materials in natural gas networks. Tech. rep. SAND2021-8820C, Albuquerque, NM (United States): Sandia National Lab. (SNL-NM); 2021.
[70] Martin ML, Connolly MJ, DelRio FW, Slifka AJ. Hydrogen embrittlement in ferritic steels. Appl Phys Rev 2020;7(4):041301.
[71] Martínez-Pañeda E, Fuentes-Alonso S, Betegón C. Gradient-enhanced statistical analysis of cleavage fracture. Eur J Mech A Solids 2019;77:103785.
[72] Ahmed B, Bahri OCE, Benattou B, Malika T. Numerical simulation of a steel weld joint and fracture mechanics study of a compact tension specimen for zones of weld joint. Frattura Integrità Strutt 2019;13(47):17–29.
[73] Navidtehrani Y, Betegón C, Martínez-Pañeda E. A simple and robust abaqus implementation of the phase field fracture method. Appl Eng Sci 2021;6:100050.
[74] Navidtehrani Y, Betegón C, Martínez-Pañeda E. A unified abaqus implementation of the phase field fracture method using only a user material subroutine. Materials 2021;14(8):1913.
[75] Martínez-Pañeda E, Betegón C. Modeling damage and fracture within strain-gradient plasticity. Int J Solids Struct 2015;59:208–15.
[76] Mandal TK, Nguyen VP, Wu J-Y. Comparative study of phase-field damage models for hydrogen assisted cracking. Theor Appl Fract Mech 2021;111:102840.
[77] Arpin K, Trimble T. Material properties test to determine ultimate strain and true stress-true strain curves for high yield steels. Tech. rep., Schenectady, NY (US): Lockheed Martin, Inc.; 2003.
[78] Souza RC, Pereira LR, Starling LM, Pereira JN, Simões TA, Gomes JaCP, Bueno AHS. Effect of microstructure on hydrogen diffusion in weld and API X52 pipeline steel base metals under cathodic protection. Int J Corros 2017;2017:e4927210.
[79] Timoshenko S, Woinowsky-Krieger S, et al. Theory of plates and shells. Vol. 2, New York: McGraw-hill; 1959.
[80] Tvergaard V, Hutchinson JW. The relation between crack growth resistance and fracture process parameters in elastic–plastic solids. J Mech Phys Solids 1992;40(6):1377–97.
[81] Kristensen PK, Niordson CF, Martínez-Pañeda E. A phase field model for elastic-gradient-plastic solids undergoing hydrogen embrittlement. J Mech Phys Solids 2020;143:104093.
[82] Williams ML. On the stress distribution at the base of a stationary crack. J Appl Mech 1957;24(1):109–14.
[83] Mandal TK, Nguyen VP, Wu J-Y. Length scale and mesh bias sensitivity of phase-field models for brittle and cohesive fracture. Eng Fract Mech 2019;217(106532).
[84] Cai L, Bai G, Gao X, Li Y, Hou Y. Experimental investigation on the hydrogen embrittlement characteristics and mechanism of natural gas-hydrogen transportation pipeline steels. Mater Res Express 2022;9(4):046512.